IMPACT OF NEW CHEVRON CONFIGURATIONS ON MIXING ENHANCEMENT IN SUBSONIC JETS

By

Sunayan Mullick

Submitted to the Faculty of the Department of Aerospace Engineering at the University of Kansas in Partial Fulfillment of the Requirements for the Degree of Master of Science in Aerospace Engineering

Committee:

_____

Dr. Ray Taghavi, Chairperson

_____

Dr. Saeed Farokhi, Committee Member

_____

Dr. Shawn Keshmiri, Committee Member

Date Defended: April 26th, 2017

The Thesis Committee for Sunayan Mullick certifies that this is the approved version of the following thesis:

IMPACT OF NEW CHEVRON CONFIGURATIONS ON MIXING ENHANCEMENT IN SUBSONIC JETS

Committee:

_____

Dr. Ray Taghavi, Chairperson

_____

Dr. Saeed Farokhi, Committee Member

_____

Dr. Shawn Keshmiri, Committee Member

Date Defended: April 26th, 2017

Abstract

A major contributor to the overall noise of an aircraft is jet noise – the noise generated by the gases exiting the exhaust nozzle of a jet engine. One approach to mitigate jet noise is through the implementation of chevron nozzles. In the present context, first, a baseline axisymmetric separate-flow nozzle, termed the 3BB model, with an external plug having a bypass ratio of 5 is analyzed. The specifications of this nozzle are taken from an acoustic study carried out at the NASA John H. Glenn Research Center. Then, various chevron configurations are added to the core and fan nozzles to produce three chevron nozzles. Of these, two are presented as modified versions of the conventional chevron nozzle and form the essence of this work. The third chevron nozzle represents the conventional chevron nozzle in use today.

For all the nozzles considered in this study, the flow conditions used represent the takeoff environment of a contemporary subsonic aircraft. The fan nozzle total pressure is set to 1.8 atm while the core nozzle total pressure is 1.65 atm. The total temperature inside the fan nozzle is set to 333.3 K while the core nozzle has a total temperature of 833.3 K. The freestream conditions are given as: static pressure = 0.98 atm, total pressure = 1.04 atm, total temperature = 298.8 K and Mach number = 0.28. For the three chevron nozzles, the core and fan nozzles have 12 chevrons each. Each chevron extends over a sector of 30 degrees of the circumference.

To carry out the study presented herein, first, computer-aided design (CAD) models of the four nozzles are created. These models are then used to carry out computational fluid dynamics (CFD) simulations with the conditions stated above. The CFD simulations are performed on STAR-CCM+. The results of the simulations carried out for the baseline nozzle are compared with existing experimental and numerical data to validate the use of STAR-CCM+ as a tool for studying jet flows. Once this step is complete, numerical simulations are carried out for the three chevron nozzles. The results from these are compared with those obtained for the baseline nozzle. The turbulent kinetic energy (TKE) and the mean axial velocity are the two main parameters that represent mixing enhancement and are focused on in this work. Since the TKE levels for a given nozzle are directly linked to the jet noise generated, the TKE is an important indication of the jet noise produced by a given nozzle. Other jet mixing parameters such as the centerline total temperature decay and the centerline velocity of the jet flow exiting each nozzle are also analyzed.

A 2-D axisymmetric grid is produced for the 3BB nozzle while a 3-D mesh is generated for each of the chevron nozzles. To reduce the computation cost, only a 30° sector of the chevron nozzles is modeled. Since the Shear Stress Transport (SST) k-ω turbulence model has been widely used in several aerospace applications, it is chosen for all simulations here as well.

The numerical analysis shows that STAR-CCM+ can successfully be used for the study of jet flows. Although some shortcomings do exist, the simulations provide a reasonable understanding of jet flows. Of the three chevron nozzles studied, the simulations demonstrate that in comparison to the baseline nozzle, all three chevron nozzles register peak values of the turbulent kinetic energy that are lower than that observed for the 3BB nozzle. The regions of highest turbulence also appear further upstream for the chevron nozzles. Compared to the conventional chevron nozzle, the two parametric designs presented in this work show a potential reduction in the peak values of the turbulent kinetic energy in their respective flows. A slight reduction in the mean axial velocities is also observed for these nozzles. Further, a close inspection of the turbulent flowfield of one of the parametric designs shows that the highest intensity turbulence in the flow is first observed at the most upstream location for this nozzle. The high levels of TKE are also confined to a smaller region in this case. Based on these results, the two parametric chevron nozzle designs demonstrate a potential to produce lower jet noise than what is observed in case of a conventional chevron nozzle.

Finally, a study of the turbulent flowfields of all the nozzles shows that the mixing between the fan and freestream shear layers still dominates the mixing in the jet flow. However, the chevrons are able to add streamwise vortices to the flow that enhance mixing between the core and fan shear layers to some extent. This promotes better mixing and as a result, the turbulence in the jet plume is reduced.

Acknowledgements

First, I would like to sincerely thank my advisor, Dr. Ray Taghavi, for his invaluable advice and support. Ever since I was an undergraduate student, I have always enjoyed your courses and consider myself lucky having taken all the courses you have ever offered.

I would also like to convey my heartfelt gratitude and appreciation to Dr. Saeed Farokhi for introducing me to the very exciting field of aircraft noise. You are an extraordinary teacher and I have learnt a lot under you. I hope to carry that education forward with me wherever I go.

Thank you to Dr. Shawn Keshmiri too for being on my graduate committee. You have always pushed me to work harder and I think that that has made me a better engineer and person.

To my parents and my sister, thank you very much for all the guidance, support, and advice over all these years. You have stood by me like a rock through the good times and the bad, and I appreciate you a lot for that. To my parents, thank you for showing my sister and me the importance of a good education. Without your hard work and dedication, I would have never been able to study aircraft, rockets, and spacecraft at the University of Kansas.

I would be remiss if I did not thank my amazing girlfriend, Neha, for her continued support throughout this time. Thank you for dealing with my long hours in the design lab and for keeping my sanity in check when I thought that I was losing it. And last but not least, I would like to thank all the friends that I made here at KU over the past seven years. You have helped me, and enriched my experience in the USA. I would have never been able to make it without you all.

Table of Contents

List of Figures

List of Tables

Nomenclature

Abbreviations

AAPL ..... Aeroacoustic and Propulsion Laboratory

AST ..... Advanced Subsonic Technologies

BPR ..... Bypass ratio

CAD ..... Computer-aided design

CFD ..... Computational fluid dynamics

CFR ..... Code of Federal Regulations

DOF ..... Degree of freedom

FAA ..... Federal Aviation Administration

FAR ..... Federal Aviation Regulations

GE ..... General Electric

GRC ..... Glen Research Center

HSR ..... High Speed Research

ICAO ..... International Civil Aviation Organization

NPR ..... Nozzle pressure ratio

P&W ..... Pratt and Whitney

PIV ..... Particle image velocimetry

RANS ..... Reynolds-Averaged Navier-Stokes

SFNT ..... Separate-Flow Nozzle Test

SFNT2K ..... Separate Nozzle Flow Test 2000

SST ..... Shear stress turbulence

TKE ..... Turbulent kinetic energy

Symbols

$\frac{dT_t}{d(x/D_f)}$ ..... Rate of change of the centerline total temperature ..... K

$\frac{dU}{d(x/D_f)}$ ..... Rate of change of the centerline velocity ..... ft/s

D..... 3BB nozzle exit diameter ..... in.

l.e.....Leading edge..... ~

S .....Sutherland constant.....K

T ..... Temperature .....K

t.e.....Trailing edge..... ~

U.....Velocity.....ft/s, m/s

x.....Distance from 3BB fan nozzle exit..... in.

μ .....Dynamic viscosity.....Pa-s

Subscripts

0.....Reference value

f ..... Fan nozzle

t .....Stagnation value

1. Introduction

Human beings have been intrigued by the ability to fly since times immemorial. Starting from the 1900s until now, the aerospace industry has made massive strides in terms of technology and speed. From the Wright brothers' first glider flight lasting only a few seconds to the biggest and fastest aircraft seen today, aircraft have made a huge impact on the world, be it economically, or scientifically.

Beginning in the 19th century, a major shift was witnessed in the modes of transportation. In the 1800s, the conventional system of transport comprised ships and boats across rivers and oceans, and carriages and wagons across thousands of miles of roads. By the 1900s, railroads were starting to develop between major junctions across the world. Trains greatly reduced the time taken to travel between cities and also helped to transport various goods with ease. However, these were still relatively slow forms of transportation. In constant search for a faster system of transportation, human beings developed an entirely new form of transportation – airplanes. Airplanes were first introduced to the world in the early years of the 20th century. In America, regional airlines began to offer scheduled passenger flights in the late 1920s. However, it was not for another 40 years before air travel truly became a popular and affordable method of travel [1].

Over the years, as airplanes became a common sight in the skies, mankind pushed to fly at higher speeds. A major obstacle was experienced when it came to crossing the sound barrier. This too, was achieved on October 14th, 1947, when U.S. Air Force Captain Chuck Yeager broke the sound barrier attaining a top speed of Mach 1.06 in the Bell XS-1 rocket research plane [2].

While aircraft have progressively evolved into the fastest modes of transport in the world, they have also presented one major problem – noise. During the early years of aviation development, some piston-engine planes produced noise that many considered a nuisance. However, it was the arrival of jet engines that increased the level of noise emanating from airplanes. The Boeing 707, first delivered in 1958, immediately became a cause for concern to the airports where it landed and took off from. Surrounding communities complained about the noisy turbojet engines. Airport authorities at Heathrow Airport in London and Idlewild (now Kennedy) Airport in New York set up noise limits in the 1960s. According to these rules, long-range aircraft were now

required to fly with less fuel and passengers in order to reduce weight so that they could climb quickly and get farther away from densely populated regions faster. As a result, some aircraft took off from Heathrow and landed at another airport in England to refuel before flying across the Atlantic Ocean. This was to ensure that these airplanes had full engine power available to them before embarking on long haul flights. This, of course, proved to be very inconvenient [3].

Following a vast number of protests and complaints by people affected by aircraft noise, the U.S. Federal Aviation Administration (FAA) finally instituted the first aircraft noise regulations as part of the Federal Aviation Regulations (FARs) in Title 14, Code of Federal Regulations (14 CFR) Part 36, "Noise Standards: Aircraft Type Certification" in 1969. FAR Part 36 went into effect on December 1st, 1969. It set the guidelines regarding noise emissions from various aircraft [4]. According to FAR Part 36, certain limits are established on the maximum noise that can be produced at an airport at three different points – two on either end of the runway, with one being under the aircraft on approach (approach point), and the other under the aircraft on departure (take-off point), and the third placed on the side of the runway next to the aircraft on departure (sideline). FAR Part 36 also established a sliding scale for allowable noise levels versus the takeoff weight for large aircraft. This meant that bigger aircraft could be noisier [3]. Figure 1.1 shows the noise measurement locations as laid out in FAR Part 36.

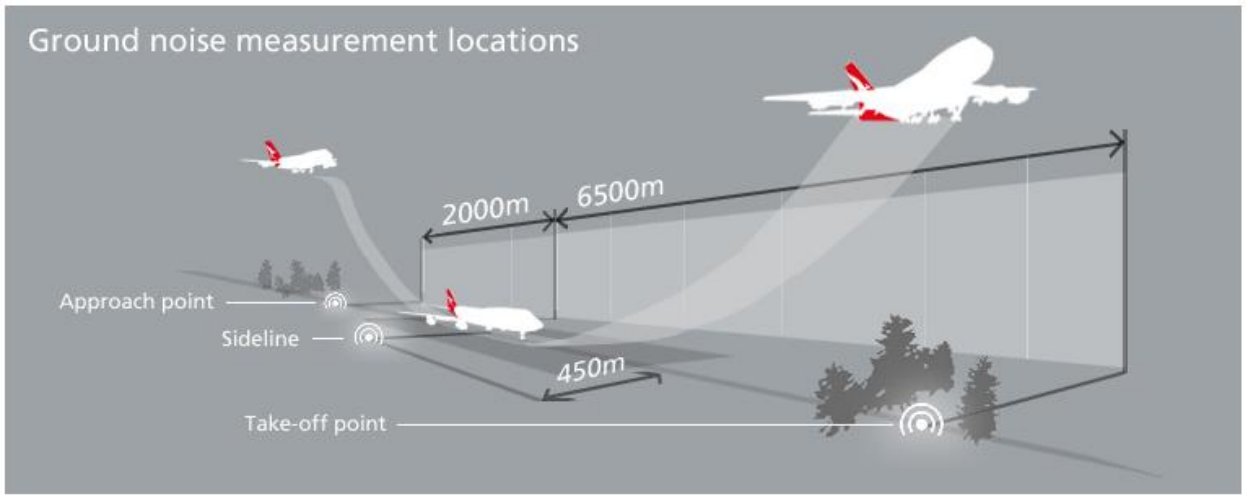

Figure 1.1: Certified Noise Measurement Locations [5]

Aircraft now comply within specified noise limits through standards or "stages." These standards are accepted worldwide and are an integral aspect of aircraft flying in the sky. They are applied when an aircraft is trying to receive its airworthiness certification. According to these rules, all

aircraft are required to either meet, or fall below the designated noise levels. For civil jet aircraft, FAR Part 36 lists four stages wherein Stage 1 applies to the loudest aircraft while Stage 4 refers to the quietest. For helicopters, two stages exist – Stage 1 and Stage 2, where Stage 2 is quieter than Stage 1. Currently, the FAA is working to adopt the latest international standards for helicopters. This will be called Stage 3 and will be quieter than Stage 2 [6]. Along with the FAA, the UN's International Civil Aviation Organization (ICAO) also works on developing new policies and adopting new standards on aircraft noise. Much of the background for the development of the Stage 4 noise standard was undertaken on an international level with the help of the ICAO. All aircraft certified in 2006 and later either meet, or exceed Stage 4 requirements.

Over the years, as the need to make aircraft quieter has increased, much progress has been made in the field of noise. With noise standards being revised from time to time, accepted noise levels from previous years have been constantly modified. As a result, the latest aircraft today are around 80% quieter that those in service about 60 years ago. Figure 1.2 shows a timeline of the change in noise emissions from aircraft since the 1950s.

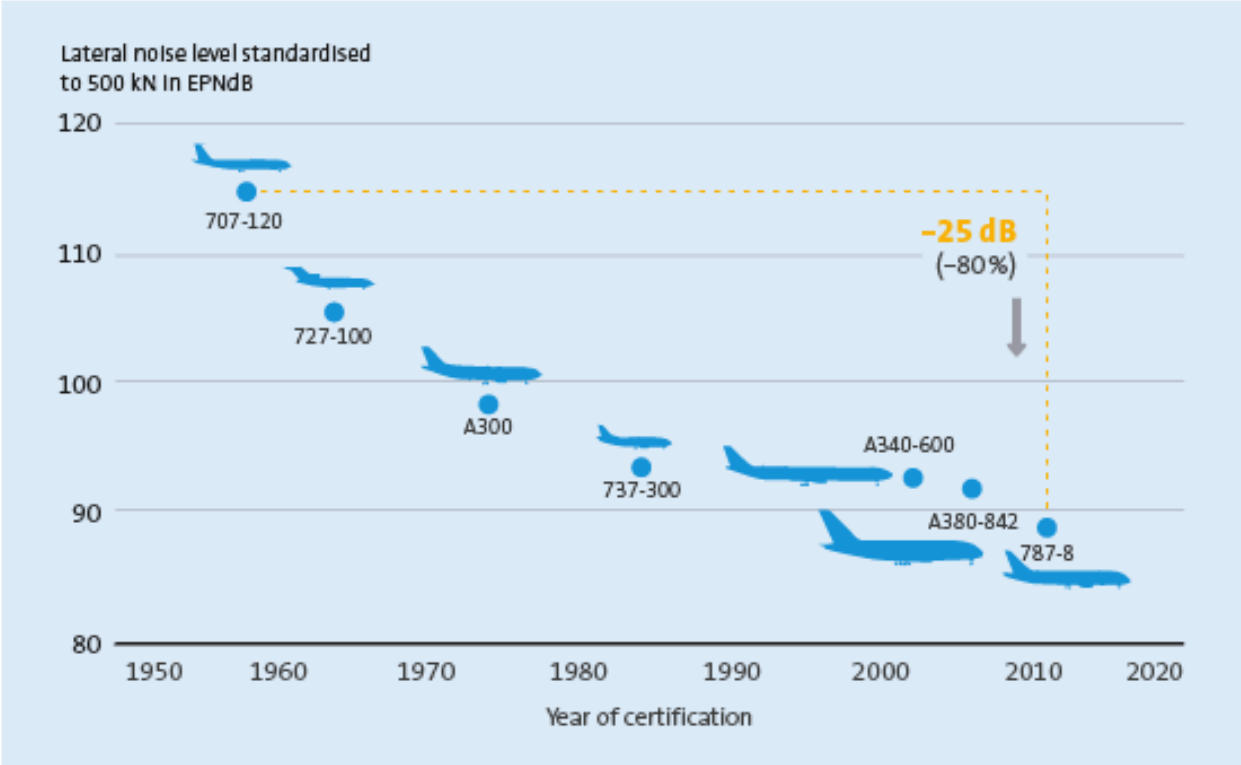

Figure 1.2: Advancements in Aircraft Noise over Time [7]

1.1 Sources of Aircraft Noise

The noise that is heard from an aircraft during various stages in its flight starting from take-off to landing is a combination of the sounds produced from its engines as well as those produced by the aircraft body as a whole. Further, the noise generated by a subsonic aircraft varies greatly from that produced by a supersonic airplane. However, in general, all noise stems from pressure fluctuations in an unsteady flow. In an unsteady flow, pressure fluctuations occur in order to balance out the fluctuations in momentum. Since all real fluids are compressible, these pressure variations are communicated to the surrounding fluid and propagate outward from the flow. These pressure waves in the surrounding fluid make up what is recognized as sound. The term 'aeroacoustics' refers to the sounds generated by aerodynamic forces or motions originating in a flow rather than by externally applied forces or motions of classical acoustics. Hence, the sounds produced by the vibration of strings on a violin become a part of classical acoustics, whereas those developed by unsteady aerodynamic forces on propellers or by the turbulent flow at the exhaust of an engine nozzle fall into the category of aeroacoustics. The term 'aerodynamic sound' was introduced by James Lighthill in 1952. It was Lighthill who laid down the foundations of the field of aeroacoustics [8].

When it comes to aircraft noise, the noise generated can be attributed to two major sources – noise emanating from the entire body of the aircraft, called airframe noise, and noise produced by the engines of the aircraft, called engine noise. Airframe noise is generated by the parts of the aircraft such as the fuselage, wings and landing gear. Engine noise, as the name suggests, is attributed to the engine. The turbomachinery inside the engine and the turbulent mixing of the exhaust gases with the surrounding air together contribute to engine noise. Jet noise refers to the noise created by the jet flow exiting the nozzle. Sometimes, in the case of turbofan engines, a differentiation is made between the noise generated by the gases exiting the fan nozzle (fan noise) and those leaving the exit of the core nozzle (jet noise). For turbojet engines, fan noise and jet noise become one and the same thing. Figure 1.3 demonstrates the various parts of an aircraft that lead to aircraft noise.

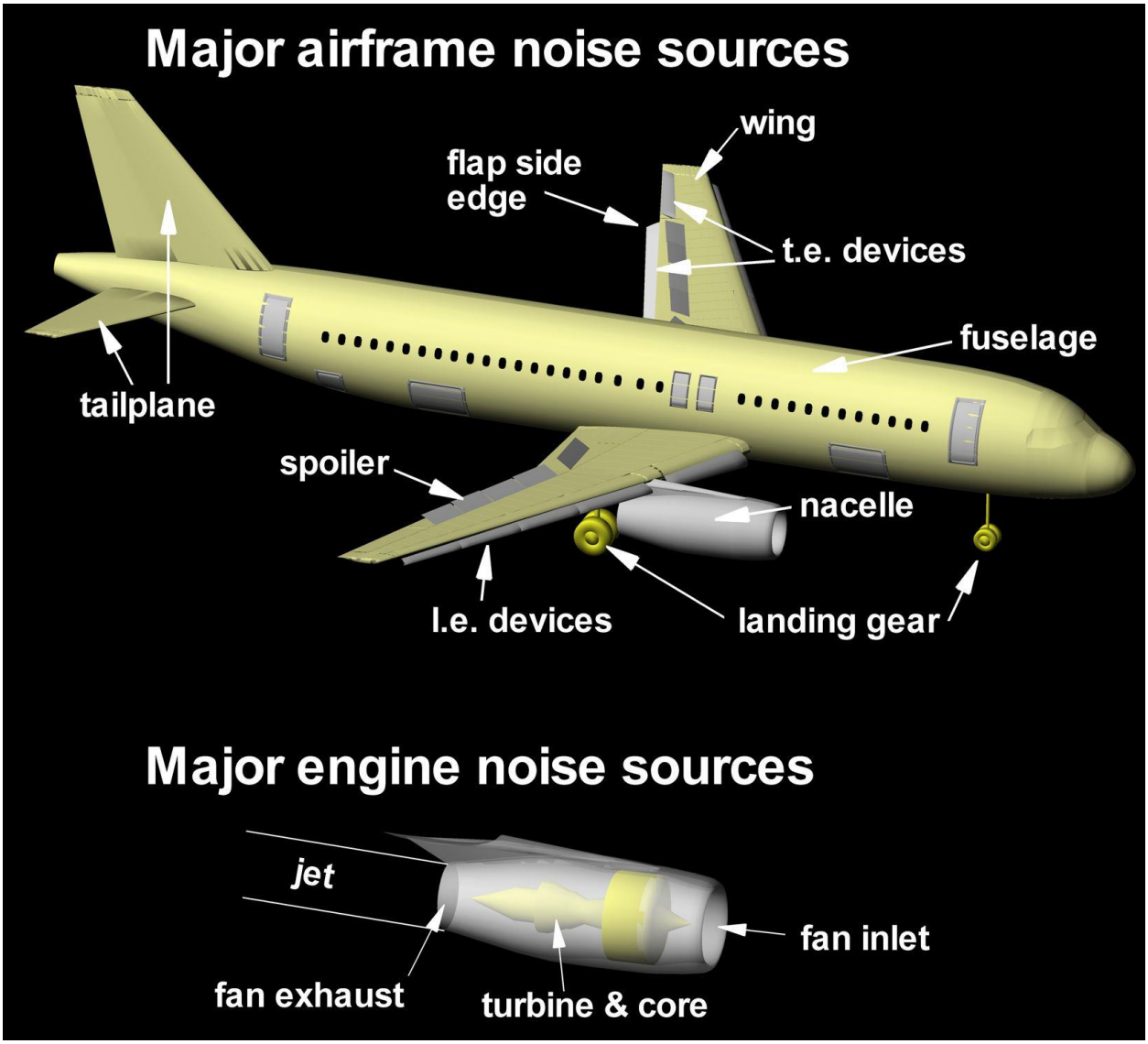

Figure 1.3: Sources of Aircraft Noise [9]

For both subsonic, and supersonic aircraft, a significant amount of noise is created during the take-off and approach phases. In addition to engine noise, external components of the aircraft such as the landing gear, slats, and flaps contribute to airframe noise. Supersonic aircraft cause additional noise in the form of sonic booms. All these sources of noise are, of course, unwanted and as a result, have become major areas of research for several decades now.

1.2 Aircraft Noise Mitigation Techniques

In the last sixty years or so, scientists and engineers have looked at various ways to tackle the problem of aircraft noise. As mentioned earlier, the take-off and approach segments are critical

in this regard since the noise generated during these greatly affect the communities situated around airports. Figure 1.4 presents a graph showcasing the distribution of noise from various components of a typical aircraft during take-off and approach.

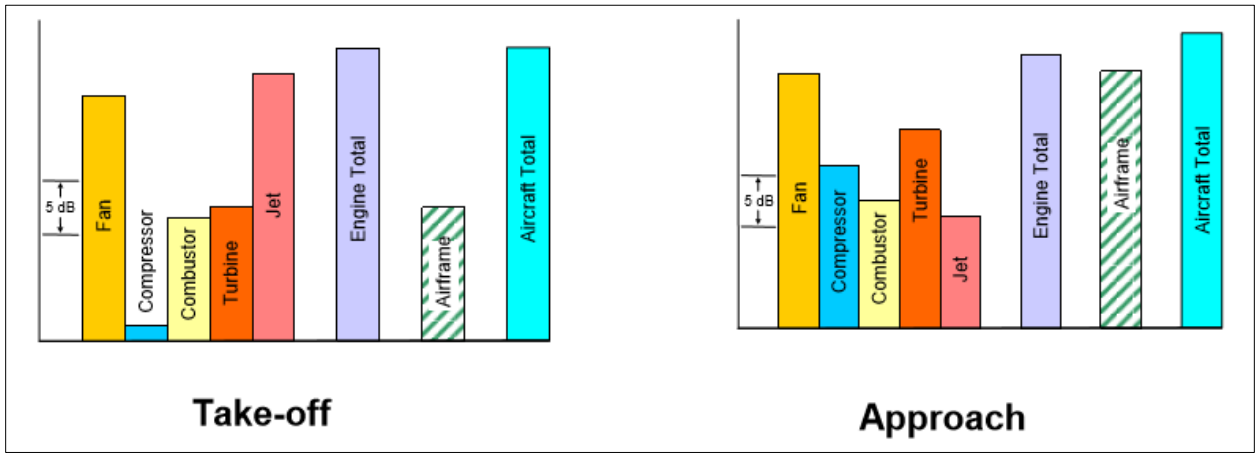

Figure 1.4: Noise Contribution of Aircraft Components during Approach and Take-Off [10]

Conventionally, acoustic liners have been used on aircraft to mitigate noise. These liners are typically applied to the internal walls of a turbofan engine nacelle. They are shaped as classical honeycombs where the outer plate is either porous or perforated. Essentially, they serve as Helmholtz resonators and help to reduce noise within an optimized frequency range. As a result, they are used to mitigate fan noise which is tonal in nature. Often, these liners comprise superimposed layers of individual liners. Depending on the number of honeycomb cell layers used between the upper and lower plates, these liners are called “2 degrees of freedom” (2DOF) or even, “3 degrees of freedom” (3DOF). Compared to liners with one honeycomb cell layer, 2DOF and 3DOF liners assist in broadening the range of frequencies to be absorbed [11]. Figure 1.5 shows a single layer perforated acoustic liner.

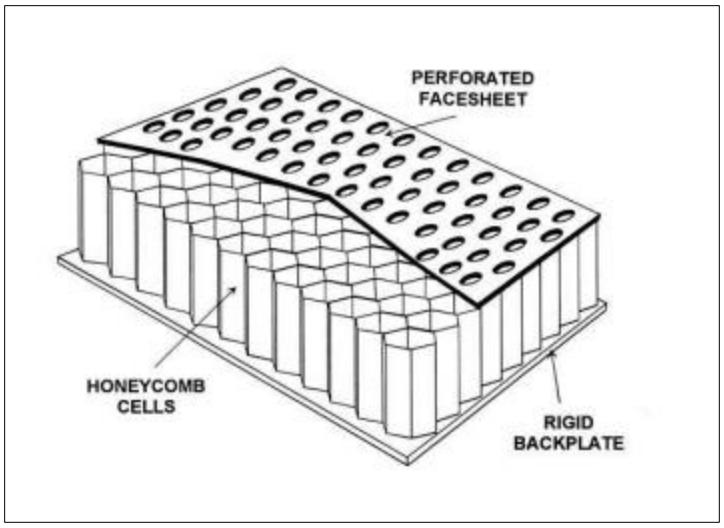

Figure 1.5: Single Layer Perforated Liner [12]

Ongoing research in aeroacoustics has also identified other methods to mitigate noise. For instance, to tackle landing gear noise, research has shown that a reduction of more than 10 dB can be achieved through the application of a complete aerodynamic fairing on the landing gear. However, this proves to be impractical and is thus, not implemented on aircraft. Figure 1.6 shows a comparison of the noise levels from a conventional landing gear of the A320 aircraft with the same landing gear with complete aerodynamic fairing.

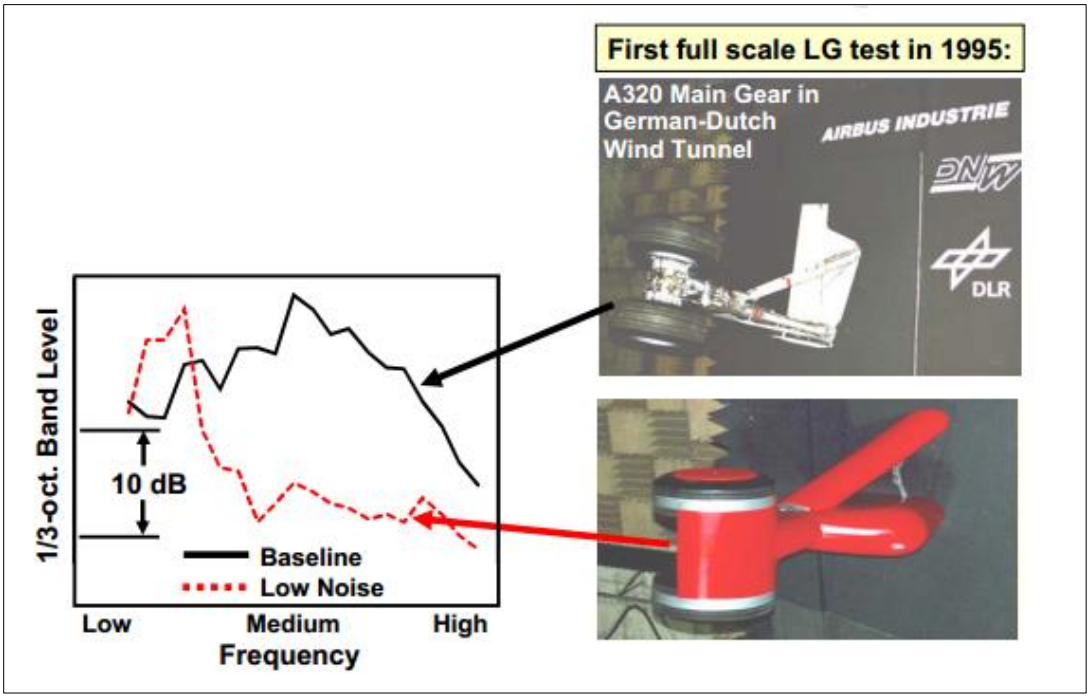

Figure 1.6: Effect of Complete Aerodynamic Fairing on the Noise from the Landing Gear of an A320 [13]

When it comes to engine noise, acoustic liners have helped to reduce some of the noise emanating from within the engine. However, a lot of work has also been done to counter jet noise. Since jet noise still remains a major contributor to the overall noise from an aircraft, various methods have been experimented with to reduce it. This is discussed in detail in the next section.

1.3 Overview

In the present work, a preliminary analysis of jet noise from a subsonic nozzle has been concentrated upon. An immense amount of work has been carried out over the years to analyze and understand this subject. This study aims to further investigate the topic and draw conclusions based on the results obtained.

2. Aircraft Engine Noise Suppression

The exhaust system, comprising the nozzle, is an integral component of a gas turbine engine. The nozzle is critical to the overall functioning of an aircraft engine since the thrust of the aircraft depends on parameters such as the design of the nozzle and the nozzle pressure ratio (NPR). An efficient nozzle is one that is able to increase the kinetic energy of the exhaust gases at the nozzle exit and match it as closely as possible with the ideal kinetic energy of the gases that would emerge if the flow expanded isentropically in the nozzle. Linked to the efficiency of a nozzle is the nozzle pressure ratio which represents an important operational parameter of a nozzle. It signifies the expansion potential of the flow from within the nozzle to the ambient air outside. Given this logic, an ideal nozzle is one that expands the exhaust gases to the air pressure outside with total efficiency, thereby maximizing thrust. Consequently, the total thrust from an engine is heavily dependent on the performance of the nozzle used.

The exhaust system of a modern aircraft is tasked with several design objectives such as low-installation drag, low-cooling requirements, low cost of manufacturing and low weight. For supersonic military aircraft, there exist the additional requirements of efficient thrust reversing and vectoring capabilities, and low radar and thermal observables. Beyond these, is the consideration of jet noise in the case of both, commercial and military transport. In the present context, the noise from subsonic jets has been concentrated upon.

2.1 Jet Noise

When a fluid flows as a jet into a stagnant or relatively slower moving background fluid, the shear formed between the moving and stationary fluids results in a fluid-mechanical instability that causes the interface to disintegrate into vortices. These vortices then travel downstream at a velocity that is of an intermediate magnitude of those of the high and low speed flows. The characteristics of the noise produced by the jet depends on whether this velocity is subsonic or supersonic in comparison to the external flow [14].

With regard to subsonic exhaust flows, as the jet exits into the ambient air, an annular mixing region forms between the jet and its surroundings. The flow in this region becomes turbulent within about one-half of the jet diameter downstream. It then spreads linearly into both, the jet

and the surrounding atmosphere until it fills the entire jet at four or five diameters downstream. The flow within the conical region that is bounded by the turbulent flow remains laminar. This region is called the potential core. Once the mixing region has filled the jet, its uniform growth ceases. It now evolves in a different way as it first passes through a transition region. Finally, at about eight diameters downstream, it transforms into a region of self-preserving flow called the fully developed region [8]. Figure 2.1 shows a graphical representation of the jet structure formed for subsonic jet flows.

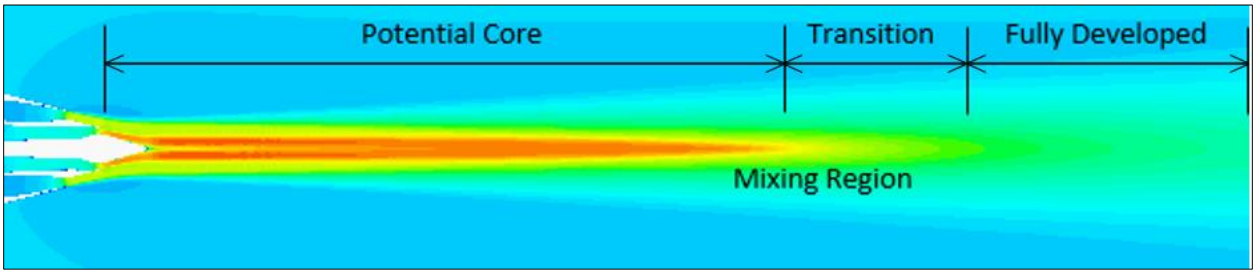

Figure 2.1: Subsonic Jet Structure

For subsonic jets, it is observed that the acoustic power per unit length approaches zero very rapidly in the fully developed region. Most of the power is emitted from the first eight or ten jet diameters, with most of it coming from the mixing region. The turbulence in the mixing region is characterized by small scale eddies that result in high frequency sounds, while the developed region showcases larger eddies generating low frequency sounds. Lighthill showed that the total sound power emitted by the jet was directly proportional to the eighth power of the jet velocity [15]. While the eighth power law, as it is sometimes referred to, has been verified to be correct for subsonic jets over a wide range of velocities, a significant departure is seen at high supersonic speeds where the acoustic power is seen to depend on the cube of the jet velocity [14].

2.2 Jet Noise Suppression

The principle of jet noise suppression is to affect change on one or more parameters of the jet acoustic power such that a reduction in sound levels is observed. For years now, various techniques to mitigate jet noise have exploited the characteristics of the jet flow itself as well as those of the observer on the ground. The audible frequency range for the human ear falls roughly between 20 Hz to 20 kHz. As a result, if the total noise power emanating from a flow is higher

than this range, the human ear is less sensitive. One way of achieving higher frequencies from a jet flow is by replacing a large nozzle with several smaller ones. This is because the angular frequency of sound waves is indirectly proportional to the jet diameter. Smaller nozzles result in smaller jet diameters as compared to the jet diameter formed in the case of a single large nozzle. This helps to shift to higher frequencies. Corrugated and lobe-type nozzles work to reduce noise by exploiting this concept. Mengle et al. [16] observed that in comparison to coaxial nozzles, lobed mixers reduced low-frequency noise at shallow angles from the jet axis, and also created the possibility of an increase in higher frequencies at steeper angles due to rapid mixing of the jet stream with the surrounding air. Figure 2.2 shows a corrugated mixer and a lobe-type nozzle.

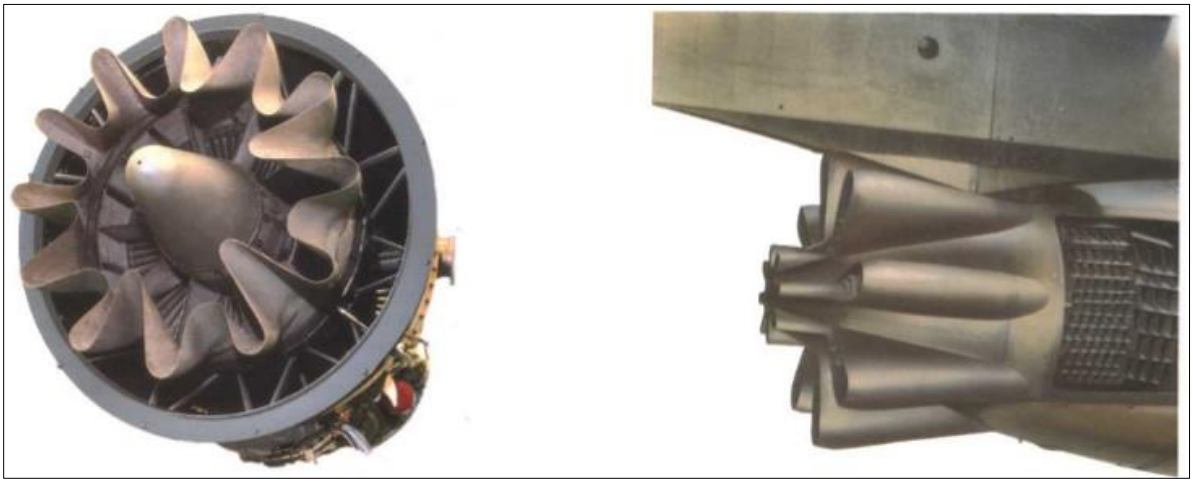

Figure 2.2: Corrugated Internal Mixer (Left) and Lobe-Type Nozzle (Right) [17]

Another important method of mitigating jet noise is by reducing the mean jet velocity. Since the acoustic power of a jet is proportional to the eighth or third power of the jet velocity (depending on whether the velocity falls within the subsonic or supersonic regime), a reduction in the jet speed can have a significant impact on the overall noise. When turbofan engines first came into effect, they were able to significantly reduce jet noise. Prior to turbofan engines, turbojet engines produced high levels of jet noise owing to the violent mixing of the exhaust with the ambient air outside. In comparison, the jet exiting out of a turbofan engine mixes with the larger bypass air flowing through the fan, thereby creating a region of more enhanced mixing. This leads to reduced levels of jet noise from a turbofan engine. Hence, the higher the bypass ratio of an engine, the lower is the noise produced from the exhaust. Figure 2.3 shows a comparison of the noise sources and levels of low and high bypass engines.

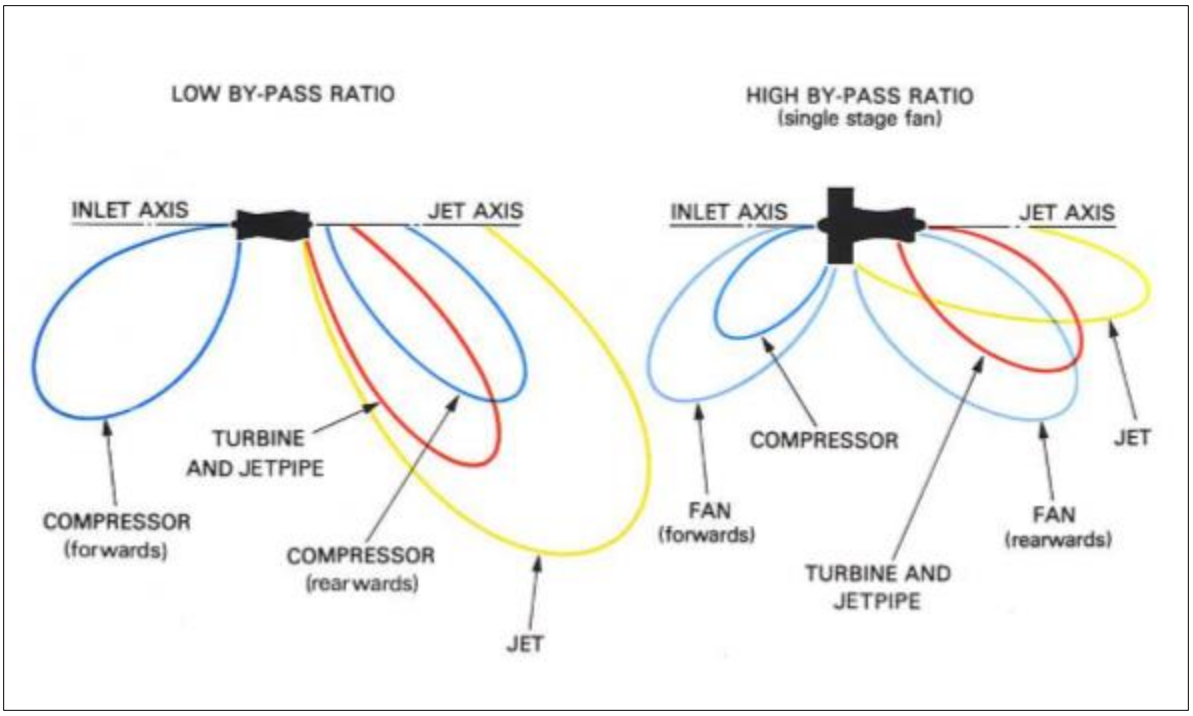

Figure 2.3: Comparison of Noise from Low Bypass and High Bypass Engines [17]

The methods discussed above have been able to successfully reduce jet noise. However, they also present unique problems. While corrugated mixers and lobed nozzles demonstrate the largest noise reductions, huge costs in performance outweigh the benefits. For example, in order to match the nozzle exit area of a conventional subsonic convergent nozzle, the total diameter of the suppressor would have to be increased by so much that significant weight and drag penalties would be incurred. Similarly, gradually raising the bypass ratio of a turbofan engine to further reduce the noise would eventually lead to such a massive and heavy engine that the engine would not be feasible anymore.

2.2.1 Chevron Nozzles

In the 1980s, experiments were carried out with laboratory-scale jets that involved having small rectangular protrusions at the nozzle exit. These protrusions, called ‘tabs’, were bent into the flow and effectively suppressed screech noise produced by supersonic jets. Bradbury and Khadem [18] observed that the tabs reduced the potential core length of the exhaust to about two diameters followed by a swift decline of the centerline mean velocity. Essentially, the tabs served as vortex generators, generating streamwise vortex pairs that enhanced the mixing of the jet stream and the surrounding air. Further, they were equally effective in both, supersonic and

subsonic conditions [19]. The improved mixing helped to lower the jet velocity and in effect, the jet noise – a direct consequence of Lighthill's eighth power law.

A parametric study was conducted at the NASA Lewis Research Center to optimize the effect of the tab geometry and the 'delta tab', a precursor to chevrons, was born. Delta tabs were triangular in shape and like tabs, penetrated aggressively into the flow. Zaman et. al [20] carried out an experimental investigation of the effect of vortex generators in the form of delta tabs on the evolution of a jet up to a jet Mach number of 1.8. The delta tabs were found to be the most effective when it came to producing streamwise vortices. Further, a plausible improvement in the jet mixing downstream was observed in going from two delta tabs spaced 180 degrees apart to four delta tabs. While tabs were found to be effective in enhancing the mixing of the exhaust and in reducing the jet plume thereby suppressing screech and broadband noise at low frequencies, usually, a penalty was incurred at higher frequencies that fell in the human hearing range for scaled-up practical nozzles. As a result, investigations into the effect of chevrons picked up speed.

'Chevron' derives from Latin and is used to describe a figure or an object in the shape of the letter 'V' or an inverted 'V'. With regard to aircraft nozzles, chevrons are the sawtooth-like patterns seen on the trailing edge of certain modern jet engines. Unlike tabs, chevrons are essentially extensions of the nozzle, ending in triangular shapes periodically appearing around the circumference of the exit. Initially, the chevrons were aligned parallel to the direction of the nozzle surface at the exit. However, later, a slight bending of the chevrons into the flow was allowed. The term 'chevron' was first employed in conjunction with the mixer-ejector nozzle studies carried out under NASA's High Speed Research (HSR) Program that began in 1990. It was later mentioned by GE Aircraft Engines (GEAE) in its proposal to NASA's Advanced Subsonic Technologies (AST) Program in 1995 [21]. The AST program was initiated by the NASA Glenn Research Center (GRC) to study jet noise mitigation techniques for separate flow nozzle exhaust systems. These were to be applied to long-range subsonic aircraft that utilized medium to high by-pass ratio engines. Several companies such as General Electric (GE) and Pratt & Whitney (P&W) submitted proposals to carry out tests with passive mixers such as tabs that would aid in noise reduction. The concepts submitted by various companies interested in the project eventually led to the creation of the Separate-Flow Nozzle Test (SFNT) program in 1997.

The SFNT program focused on engines that comprised two nozzles – one fan nozzle, and one core nozzle. Since two separate streams exited the entire nozzle before entering the air outside as one single stream, these nozzles were called separate-flow nozzles. GEAE and P&W won contracts under which scaled models of separate-flow nozzles along with a range of noise suppression devices were to be designed, built and studied. Under the SFNT program, five baseline nozzle models were chosen, each varying in either the configuration or in terms of the bypass ratio (BPR). Bypass ratios of 5 and 8 were chosen for the study since they represented the BPRs of engines at the time and also reflected the BPRs of future commercial engines. Both, GEAE and P&W, provided designs for various configurations of chevrons and tabs, and a combination of other mixers as well. The study concluded that in comparison to the baseline nozzles, several other exhaust systems that employed mixers such as chevrons and tabs were able to provide a noise reduction of over 2.5 dB at take-off with less than 0.5% loss in thrust at cruise at a simulated flight speed of Mach 0.8 [22].

The acoustical analysis of various nozzles and mixers in the SFNT program was conducted at the NASA Lewis Research Center Aeroacoustic and Propulsion Laboratory (AAPL). This involved the use of a microphone array set up around a nozzle that measured the frequencies produced by the jet exhaust. The experimental setup was aided by CFD simulations. While CFD simulations could provide results that could be compared with the available experimental data, scientists and engineers were in a dilemma when it came to choosing the right criteria to correlate the results from CFD with a reduction in noise. Since not much was known about the mechanism of jet noise, the CFD results were an issue since the acoustic benefits of the chevrons could not be properly understood. Theoretically, a rapid decay of the jet plume would reduce the noise produced downstream and hence, reduce the low-frequency noise. However, a region of high turbulence near the end of the nozzle had the potential to increase the high-frequency noise. This was clearly difficult to interpret from the simulation results. Eventually, the trends in the profiles of the turbulent kinetic energy (TKE) were used as guidelines – nozzles with higher TKE were expected to produce more noise and vice versa [21]. Although some uncertainty existed in interpreting results this way, the TKE profiles still served as important parameters and were used to study different chevron designs.

Saiyed, Mikkelsen and Bridges [23] studied the acoustical characteristics of typical high BPR engines attached with tabs and chevrons in various configurations. The acoustic tests were conducted at the NASA Glenn (formerly Lewis) AAPL and the acoustic data obtained by implementing the mixing devices was compared to that seen on a regular engine with no mixing devices. Out of all the configurations analyzed, tabs were found to be inefficient in reducing the jet noise. Further, altering only the fan nozzle did not provide much of a noise benefit, but fitting only the core nozzle with the mixing devices helped to mitigate the jet noise considerably. Among the chevron configurations tested on the core nozzle, the ones where the chevrons protruded into the core nozzle flow demonstrated a larger noise reduction in comparison to when they did not penetrate the flow. However, the highest reduction in noise was found by using chevrons simultaneously on both, the fan and core nozzles. Apart from the acoustic analysis, performance characteristics of the different configurations were also analyzed and compared with those of the baseline nozzle. The performance characteristic of each engine was taken at Mach 0.8 and was measured in terms of the cruise thrust loss in points. Since jet noise reduction with passive mixing devices comes with some level of loss in thrust, the various configurations were analyzed to see which ones demonstrated the least amount of loss in thrust. Overall, it was found that the chevrons generally performed better than the tabs in this regard. Another interesting find was that cruise thrust losses seen from simultaneously modifying both, the fan and core nozzles, were not additive. That is, the cruise thrust loss from adding chevrons to only the fan or core nozzle did not add up to give the total loss in cruise thrust when there were chevrons on both nozzles.

While the SFNT program proved that mixing enhancement devices were in fact capable of reducing jet noise, there was a need to further validate the results. This was due partly because measuring the turbulence of hot, high-speed jet flows was a very difficult task and there was the added need to understand the correlation between turbulence and aeroacoustic noise. To understand these issues, a test program called the Separate Nozzle Flow Test 2000 (SFNT2K) was carried out in the summer of 2000. This was the first time that the Particle Image Velocimetry (PIV) technique was employed to study jet flows. The PIV method involved the study of turbulence through optical means and more significantly, provided a non-intrusive way to analyze jet flows. The technique proved to be groundbreaking in that it offered two major advantages – it helped researchers get a better understanding of turbulence and also assisted them

in analyzing exactly how turbulence could be altered to obtain reductions in jet noise. For the PIV analysis part of the SFNT2K program, three nozzles were covered in detail. These comprised a baseline axisymmetric nozzle from the SFNT program, a second nozzle with 12 chevrons on the core nozzle with the chevrons simultaneously bent into the core and fan flows, and a similar third nozzle with 24 alternating tabs on the core nozzle. The latter two nozzles were chosen since they had demonstrated the most potential in the SFNT program. The study showed that the flow field of the baseline nozzle extended up to eight fan diameters with a higher mean velocity than that observed for the other two nozzles. In contrast, the nozzles with the mixing devices had their flow fields confined to within six fan diameters. Further, the chevrons and tabs were able to reduce the turbulent kinetic energy in the jet mixing region [24]. The PIV data obtained for the three nozzles was also compared with the velocity and turbulence measurements obtained from CFD calculations [25]. Overall, the results matched generally well and while CFD was a helpful tool in validating data, the PIV technique established itself as a very effective means in gathering turbulence data from hot, jet flows.

Kenzakowski et al [26] built on the work performed during the AST program and carried out numerical simulations on laboratory-scale separate-flow nozzles to better understand the role of mixers in jet noise reduction. Modifications in the form of chevrons and tabs were made to a baseline axisymmetric nozzle and CFD simulations were carried out using the CRAFT structured grid Navier-Stokes code which were then compared with available experimental data. The three nozzles selected for this study were the same as those chosen for the work carried out in [24]. It was observed that for all three nozzles – the baseline nozzle, the nozzle with chevrons, and the nozzle with tabs – the mixing of the fan stream shear layer with the freestream shear layer dominated the turbulence in the jet plume. For the baseline nozzle, the mixing between the core and fan streams was observed to be weak owing to the lower ratio of velocities between the two streams. On the other hand, the chevrons and tabs were able to introduce vorticity into the flow that consequently enhanced the mixing between the core and fan flows. In general, the numerical solutions were found to be in good agreement with the experimental results. Koch, Bridges and Khavaran [27] analyzed the same three nozzles at NASA Glenn using the WIND solver to assess the code's potential in studying jet noise. The results of their tests were compared with the results from the CRAFT code reported by Kenzakowski et al [26] as a means to compare both

numerical solvers. Finally, the computational results from both codes were validated against the PIV results obtained in [24].

By now, while it had been established that chevron nozzles had the potential to reduce jet noise, a deeper analysis was needed regarding the chevron geometry so that scientists and engineers better understood the effects of the chevrons' geometric parameters on noise. Studies like the one shown in [23] had shown that slightly altering the chevron geometry so that the chevrons penetrated the flow resulted in a plausible reduction in noise. In this regard, a trade-off had to be made. Like tabs, if the chevrons were to penetrate the flow in an aggressive manner, then an increase in the high-frequency noise would be the outcome. On the other hand, they were absolutely necessary to reduce the low-frequency noise while preventing a large increase in the high-frequency noise. As a result, there was a need to figure out if an optimized design of chevrons could be achieved in order to have the most beneficial noise reductions. Bridges and Brown [28] carried out a parametric study of chevrons on single-flow nozzles under both, cold and hot, conditions to gain an in-depth understanding of the relationship between the chevron geometry and the resulting noise. The acoustic measurements were taken by a microphone setup and the PIV technique was utilized to validate the experiments. It was observed that for a constant chevron count and penetration, varying the length of the chevrons did not appear to influence noise to a great deal. Further, as had previously been established for separate-flow nozzles, and as was expected, chevron penetration proved to have a major impact on single-flow nozzles here too. In this case, the increased penetration into the flow significantly shortened the potential core for the hot jet and a relatively rapid decrease in the jet centerline velocity was also observed. The study also demonstrated that a high number of chevrons could reduce low-frequency noise without incurring the penalty of an increase in higher frequencies.

Callendar, Gutmark and Martens [29, 30] conducted similar tests on separate-flow nozzles with chevrons at the University of Cincinnati Nozzle Acoustic Test Facility to investigate how the number of chevrons and chevron penetration into the flow affected jet noise. The study aimed to understand the physical mechanisms through which chevrons were able to successfully reduce noise. The tests showed that both, the number of chevrons and chevron penetration, were responsible for achieving a decent decrease in noise thereby demonstrating that the mitigation of jet noise was a direct consequence of the coupling of both parameters. However, of the two, the

penetration of the chevrons into the flow had a more impactful influence. Chevron penetration was found to be the main geometric factor and affected the noise at all measured frequencies while the number of chevrons was a secondary factor that mainly influenced higher frequencies. Additionally, the results of this study also showed that the noise benefits provided by a particular configuration of chevrons were heavily dependent on the difference in the velocities of the core and fan streams. A high velocity difference was likely to induce an aggressive kind of mixing between the two flows resulting in an increase in high-frequency noise. The tests concluded that while chevron nozzles were most useful at lower frequencies, the design of chevrons needed to be very specific to a given application.

After years of theoretical, experimental and numerical research on chevron nozzles, flight tests were conducted in 2001 with various configurations of chevron nozzles being incorporated on NASA's Learjet 25 research aircraft and Honeywell's Falcon 20 test plane [21]. Later, GEAE and Boeing carried out their own tests. In each case, the noise data from the chevron nozzles was compared with that from a baseline nozzle without chevrons and the results were encouraging. Besides the benefit chevron nozzles provide in terms of noise, they are much lighter in weight compared to other mixers such as lobed mixers. Further, since they are simply extensions of the nozzle, they are also easy to manufacture and maintain. For these reasons, they can now be seen employed on jet engines such as General Electric's GEnx-2B67 that powers the Boeing 747-8 and Rolls Royce's Trent 1000 used on the Boeing 787 Dreamliner. Figure 2.4 shows the chevrons on the GEnx-1B jet engine seen here on Air India's Boeing 787.

Figure 2.4: Genx-1B Engine on Air India's B787 Dreamliner [31]

2.3 Objectives

Several studies have been done to understand how the geometric characteristics of chevrons affect the resulting noise from separate-flow nozzles. While these have shown how chevron penetration into the flow and the number of chevrons together affect the turbulence in the jet flow, the shape of the chevron itself has also been taken into consideration in this regard. For instance, Kanmaniraja et al [32] performed a parametric study of chevrons of different shapes on a supersonic nozzle and compared the resulting acoustics to those observed for a baseline nozzle with no chevrons. The work presented here aims at analyzing the resulting turbulence and jet flow as the shape of the chevrons is altered from the current conventional geometry. For this purpose, the new design of the chevrons is first modeled using CAD following which, CFD calculations are performed. Finally, the results of this analysis are compared with those for a baseline nozzle as reported in the literature review.

3. Design Methodology

In this section, the design procedure followed for the present work is outlined. First, the geometries of all the nozzles analyzed are laid out. Then, using CFD, the baseline nozzle is studied and the results are compared with the available data from the literature survey. Following this, a numerical analysis of the chevron nozzles is performed and the data obtained is compared with that of the baseline nozzle.

Before moving onto the next section, it is important that the terminology used for the nozzles be explained. The nozzles analyzed here are named in a similar fashion as the procedure used for their nomenclature during the SFNT program. The baseline nozzle for this work is called the '3BB' nozzle. The '3' in 3BB refers to the third out of five nozzles chosen as baseline configurations during the SFNT program. The first 'B' signifies that the core nozzle has undergone no modifications and is not implemented with any mixing devices thereby meaning that it is the baseline geometry for the core nozzle. The second 'B' shares the same baseline definition but represents the fan nozzle.

If either the core or the fan nozzle in the 3BB model were to be fitted with chevrons, the appropriate 'B' in 3BB would be replaced by the letter 'C'. Further, if the chevrons used were bent into the flow, then, instead of 'C', the letter 'I' would be used to signify that the chevrons bent inwards. For instance, during the SFNT program, the '3C12B' nozzle denoted that the 3BB nozzle now had 12 chevrons on the core nozzle while the fan nozzle remained in its baseline configuration. Similarly, '3I12C24' meant that there were 12 inward-bent chevrons on the core nozzle and 24 chevrons on the fan nozzle that were parallel to the direction of the fan cowl at the exit.

All nozzles studied here have external plugs and a BPR of 5. The nozzles with chevrons are modifications of the 3BB model.

3.1 Geometry of Nozzles

3.1.1 Baseline Nozzle (3BB)

The baseline nozzle chosen for the present work is Model No. 3 as reported in [22]. This nozzle, referred to as the 3BB configuration, was the main nozzle on which mixing enhancement devices were tested for both, the core and fan nozzles, during NASA's SFNT program. This nozzle will form the basis of all comparisons here. It is a laboratory scale version of an axisymmetric, separate-flow nozzle. It comprises an external plug and has a BPR of 5. The plug angle is about 16°. The core cowl exit diameter is 5.156 in. and the core cowl external boattail angle is approximately 14°. The core cowl exit plane is located 4.567 in. downstream of the fan nozzle exit plane. Figure 3.1 shows the 3BB nozzle created in CAD.

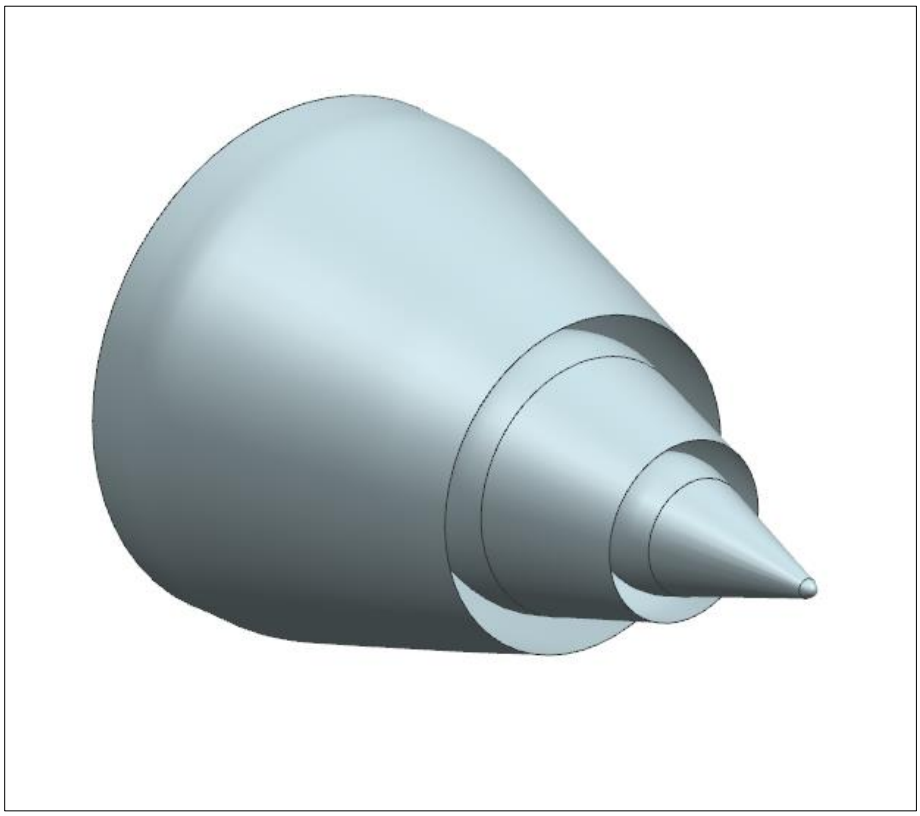

Figure 3.1: CAD Model of 3BB Nozzle

3.1.2 Nozzle with Inward-Bent Chevrons on Core and Fan Nozzles (3I12I12)

As has been reported earlier, the penetration angle of chevrons makes a huge difference when it comes to aeroacoustics. Further, as shown in [23], the greatest noise benefit was observed by

employing chevrons on both, the core and fan nozzles. Hence, to incorporate both these characteristics, the 3I12I12 model was chosen as one of the candidates for the present work. For this nozzle, the chevrons bend 4.5° into the flow with respect to the direction of flow at the nozzle exit in the absence of chevrons. The core and fan nozzles are equipped with 12 chevrons each with each chevron occupying a 30° sector of the respective circumference. The chevron geometry laid out in [22] was used as a reference to design the chevrons. Figure 3.2 shows a schematic of the geometry of a chevron.

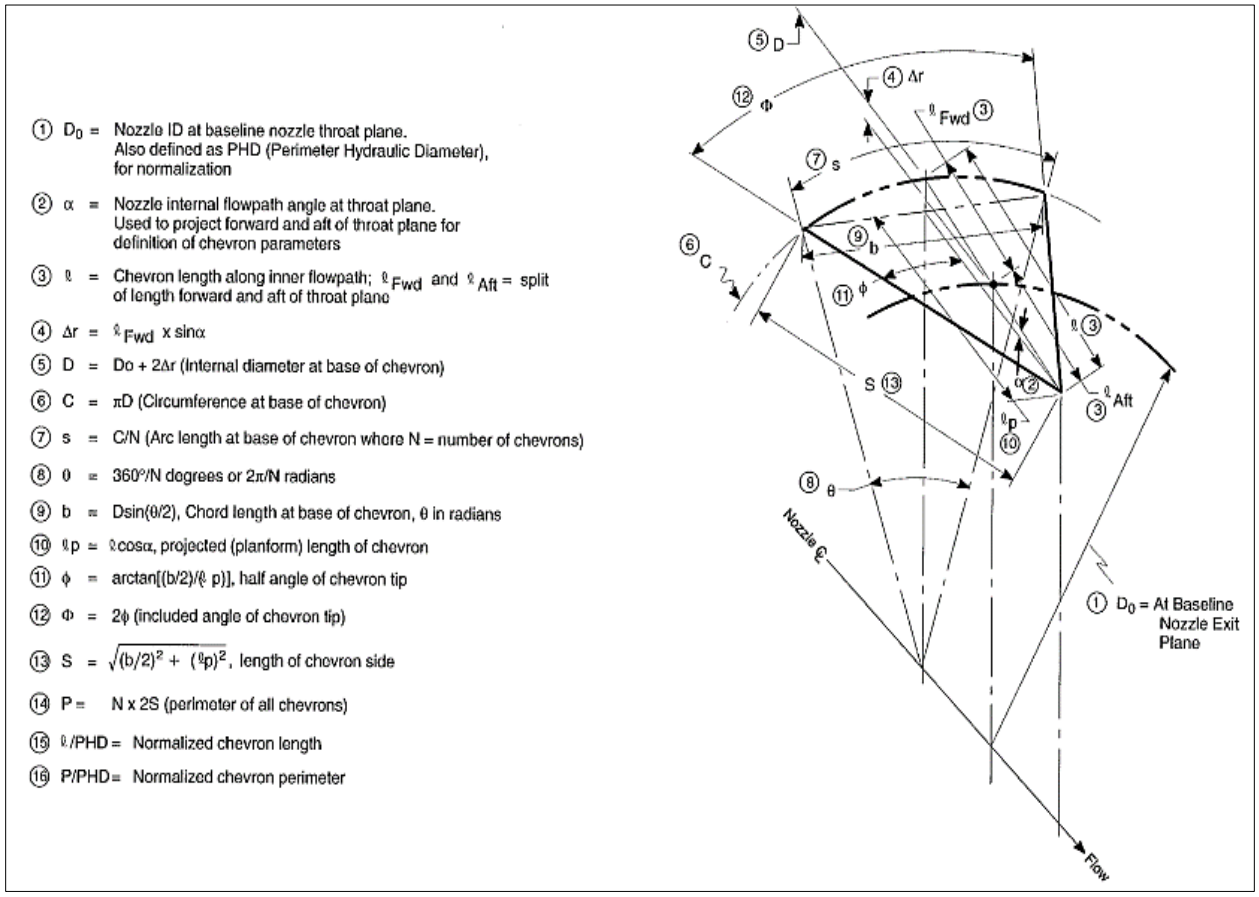

Figure 3.2: Chevron Geometry and Nomenclature [22]

Figure 3.3 shows an image of the 3I12I12 nozzle.

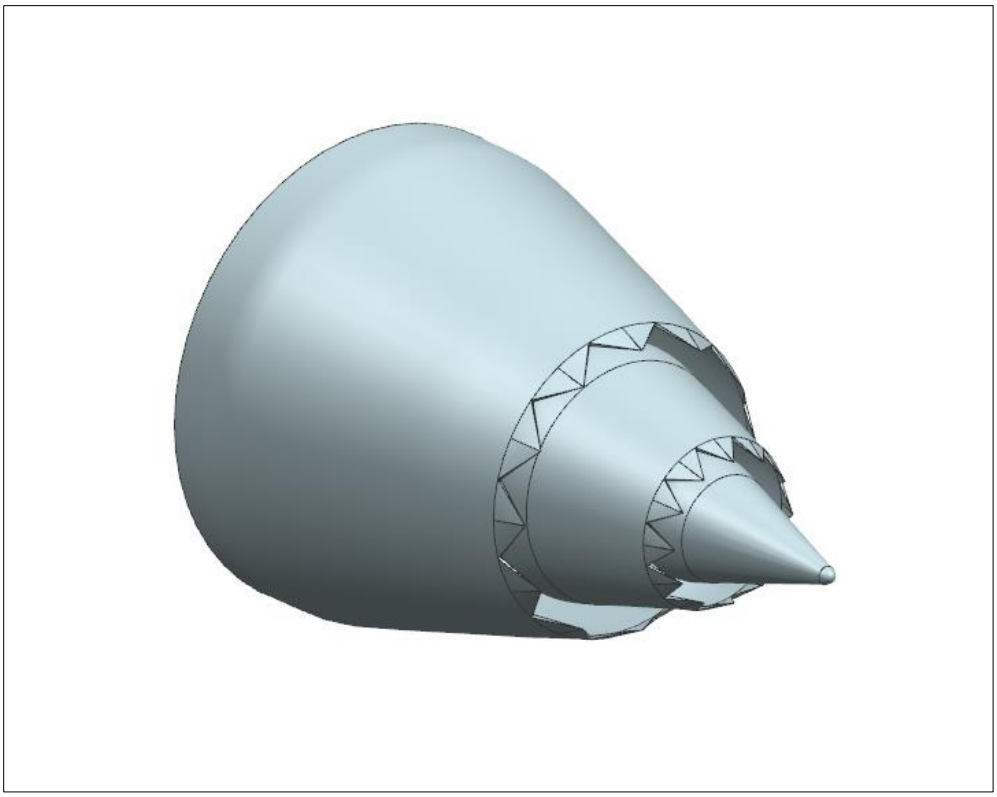

Figure 3.3: CAD Model of 3I12I12 Nozzle

3.1.3 Nozzle with Inward-Bent Twisted Chevrons

The ‘twisted’ chevrons form the essence of the analysis presented in this work. As has been mentioned previously, the basic working principle of chevrons is that they introduce streamwise vortex pairs into the flow and enhance mixing within the jet plume thereby leading to a reduction in turbulence in the ensuing fluid. These streamwise vortices that are formed, are created as counter-rotating pairs from each chevron. While chevrons have been very successful in reducing jet noise, one can question whether any further modifications could be made to the conventional chevron design to achieve an even greater reduction in jet noise. That question is looked into here through the application of ‘twisted’ chevrons. Here, the chevrons are twisted more towards one direction rather than being symmetric like the chevrons in use today. The idea behind the twist of the chevrons is that the flow coming out of the nozzle will attain a swirl that is in the direction of twist. In this case, it is of the opinion that stronger vortices are formed on one side of the chevrons than the other. To investigate if this truly has any effect on the turbulence in the flow, the twisted chevrons are first modeled on CAD following which, CFD is used to analyze the resulting jet flow.

In this regard, the terminology used before for the chevrons is slightly changed. Instead of using the letter ‘C’ to denote conventional, symmetric chevrons, ‘Tw’ is used to denote the twisted chevrons. The subscripts ‘L’ and ‘R’ are used to denote left and right twisting chevrons, respectfully. The left and right directions here are based on looking directly at the nozzle exit from the front. For the twisted chevrons, two models are created. For both models, the chevrons are applied to both, the core and fan nozzles. Further, like the 3I12I12 model, here too, the chevrons bend 4.5° into the flow and are 12 in number on each, the core and the fan nozzle. The letter ‘I’ is used here again to signify the inward bend of the chevrons.

Apart from the obvious changes made to the geometry of the chevrons in the 3I12I12 nozzle, the twisted chevrons still use Figure 3.2 as a reference for their design.

3.1.3.1 3ITw12$_R$ITw12$_R$

Figure 3.4 shows an image of the 3ITw12$_R$ITw12$_R$ nozzle.

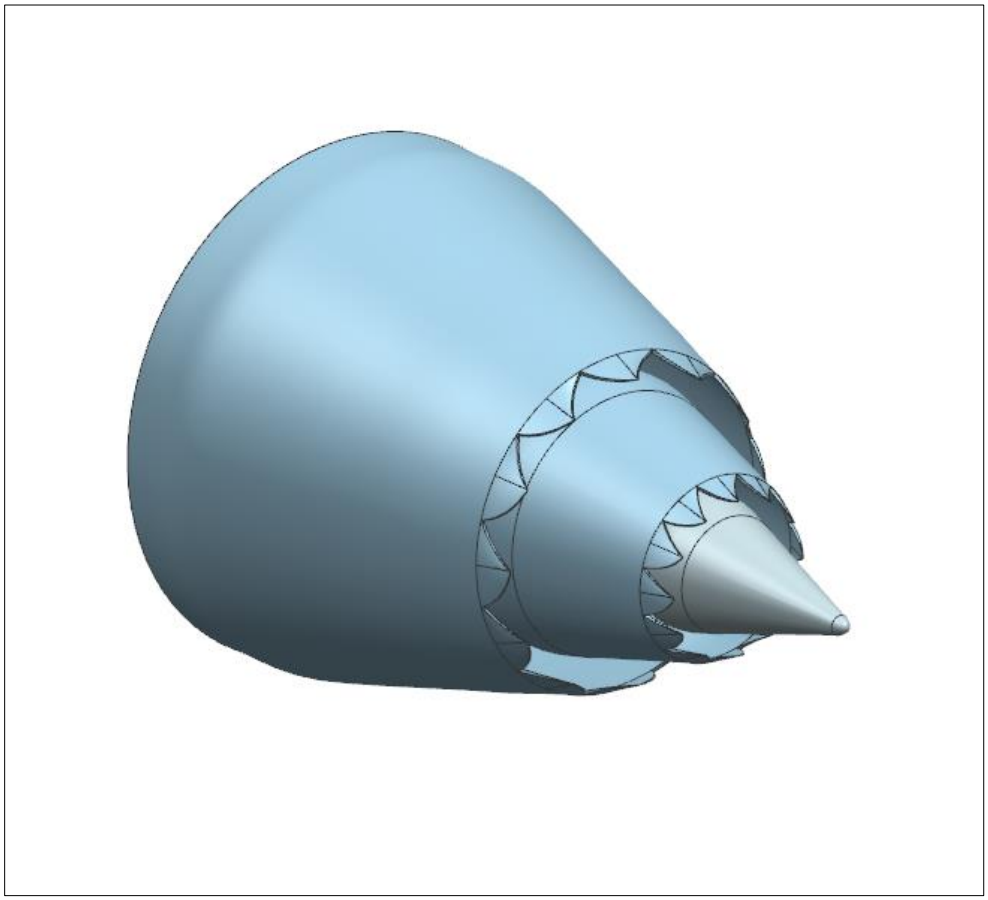

Figure 3.4: CAD Model of 3ITw12$_R$ITw12$_R$ Nozzle

3.1.3.2 3ITw12$_R$ITw12$_L$

Figure 3.5 shows an image of the 3ITw12$_R$ITw12$_L$ nozzle.

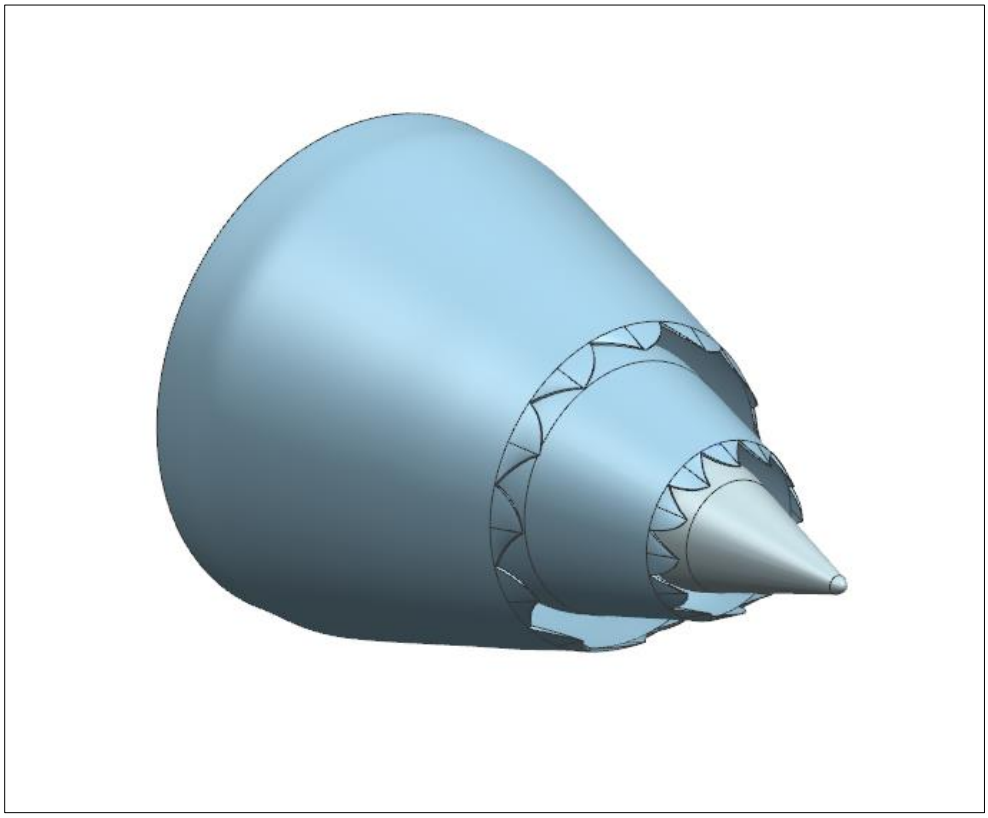

Figure 3.5: CAD Model of 3ITw12$_R$ITw12$_L$ Nozzle

3.2 Numerical Procedure

This section describes the computational methodology involved in studying the flow from the nozzles. First, variables such as the pressure and temperature in the nozzle environment are outlined. Then, the CFD methods implemented in the present work are described. Finally, the results obtained from the computations are presented.

3.2.1 Flowfield Conditions

To carry out numerical analyses on the nozzles, the surrounding environment in and around the nozzles must be known. For this purpose, the flowfield conditions are chosen to correspond to the Power Point 21 operating conditions as described in [26]. These conditions represent the

takeoff power setting of a typical subsonic medium to large commercial transport aircraft [24]. Table 3.1 describes these conditions.

Table 3.1: Flowfield Conditions for CFD Analysis

Parameter	Core Nozzle	Fan Nozzle
Total Pressure (atm)	1.65	1.80
Total Temperature (K)	833.3	333.3
Freestream Static Pressure (atm)	0.98	
Freestream Total Pressure (atm)	1.04	
Freestream Total Temperature (K)	298.8	
Freestream Mach Number	0.28	

3.2.2 CFD Analysis

3.2.2.1 Overview of CFD Setup

The CFD simulations in this study were performed on STAR-CCM+ [33]. Since the flow involved in each case falls in the compressible regime, the coupled flow solver was used. The coupled flow model simultaneously solves the equations of conservation of mass, momentum, and energy by implementing a pseudo-time-marching approach [34]. All simulations were run under steady-state conditions.

Several studies have been conducted over the years on the robustness and accuracy of various turbulence models in predicting jet flows. Further, these studies have been performed on various CFD software to gain an insight into how the results from a particular software compare with experimentally available data. Thirumurthy [35] used ANSYS FLUENT [36] to compare various Reynolds-Averaged Navier-Stokes (RANS) based turbulence models for the study of noise suppressing nozzles for a business class supersonic aircraft. For the aeroacoustic analysis presented in [27], Koch et al used the WIND solver with the k-ω Shear Stress Transport (SST) turbulence model and compared the results obtained with those determined by Kenzakowski et al [26] who used the CRAFT code with the standard k-ε turbulence model. The decision to use a particular turbulence model is one that is dependent on the user and on the application. For the purpose of the work presented herein, the SST k-ω model was used. The k-ω turbulence model is a two-equation model that offers a huge advantage in that it is able to resolve boundary layers under adverse pressure gradients [34]. The SST k-ω model, in particular, was developed to

accurately analyze aerodynamic flows. Prior to this turbulence model, the otherwise popular k- ε model had failed at properly capturing the behavior of turbulent boundary layers leading up to separation [37]. In the aerospace industry, the SST k-ω turbulence model is used widely today to study viscous flows and turbulence. Although originally developed for aerospace applications, the SST k-ω turbulence model is now used extensively in other areas as well.

In order to resolve the boundary layer next to the walls, it is important to ensure that the y+ values fall within the desired range. The SST k-ω turbulence model can be used in conjunction with the low y+ range, high y+ range and the hybrid all y+ approach. For the numerical procedure carried out in this case, the high y+ approach was implemented and it was ensured that the y+ values fell in the turbulent region of the boundary layer, i.e., between 30 and 300. This helped to reduce the overall computational cost.

For the simulations performed herein, a perfect gas equation of state ($\gamma = 1.4$) was assumed. Further, in keeping the study as close to possible with the numerical analyses conducted on separate-flow nozzles and shown previously in the review of available literature on the same, a constant turbulent Prandtl number of 0.7 was used. To account for the viscosity of air, Sutherland's Law was implemented in STAR-CCM+. Sutherland's Law is stated as follows:

$$\frac{\mu}{\mu_0} = \left(\frac{T}{T_0}\right)^{\frac{3}{2}} \left(\frac{T_0+S}{T+S}\right) \tag{3.1}$$

As is evident from Equation 3.1 shown above, Sutherland's Law helps to calculate the dynamic viscosity (μ) of a fluid at a given temperature (T). Since the dynamic viscosity of a material is dependent on the temperature, Equation 3.1 provides a method to automatically update the viscosity as the temperature varies. In the equation given, 'μ_0' and 'T_0' are the reference temperature and viscosity, respectively, while 'S' represents the Sutherland constant. Table 3.2 presents the values of these parameters in the present study

.

Table 3.2: Reference Values Used in Sutherland's Law

Reference Property	Value
Reference Viscosity, μ_0 (Pa-s)	1.716E-5
Reference Temperature, T_0 (K)	273.15
Sutherland Constant (K)	111

All CFD simulations performed in this work were carried out on STAR-CCM+ v. 11.02.010 on the Advanced Computing Facility (ACF) cluster at the University of Kansas. The ACF cluster runs on LINUX and comprises a total of 458 nodes.

3.2.2.2 Baseline Nozzle (3BB)

Since the 3BB nozzle was axisymmetric, a 2-D axisymmetric mesh was created. The quadrilateral mesher was chosen for this purpose. Wall functions were employed to resolve the viscous wall effects effectively ensuring that the y+ values fell between 30 and 300. A wake refinement region was added immediately downstream of the nozzle to ensure that the jet flow exiting the nozzle was properly captured. The mesh consisted of a total of 0.69 million cells. Figure 3.6 shows a close-up of the mesh generated for the 3BB nozzle.

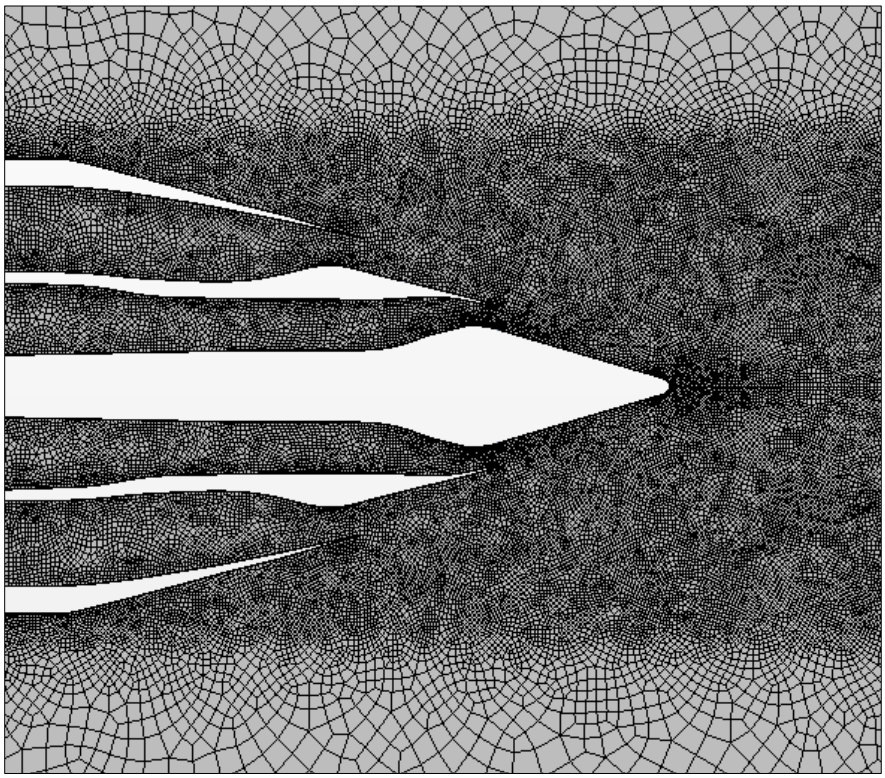

Figure 3.6: Close-Up of 2-D Axisymmetric Mesh for the 3BB Nozzle

The boundary conditions here were defined as axis along the centerline, stagnation inlets for the inlets to the core and fan nozzles, freestream for the boundary right above the fan nozzle, slip wall along the outer upper surface of the domain, and pressure outlet at the exit of the domain. The nozzle surfaces were modeled as walls and all wall boundaries were considered to be adiabatic. The domain extended 11.25 fan nozzle exit diameters in the radial direction and 54.3 fan nozzle exit diameters downstream of the external plug tip. Figure 3.7 presents an image of the domain with the defined boundary conditions.

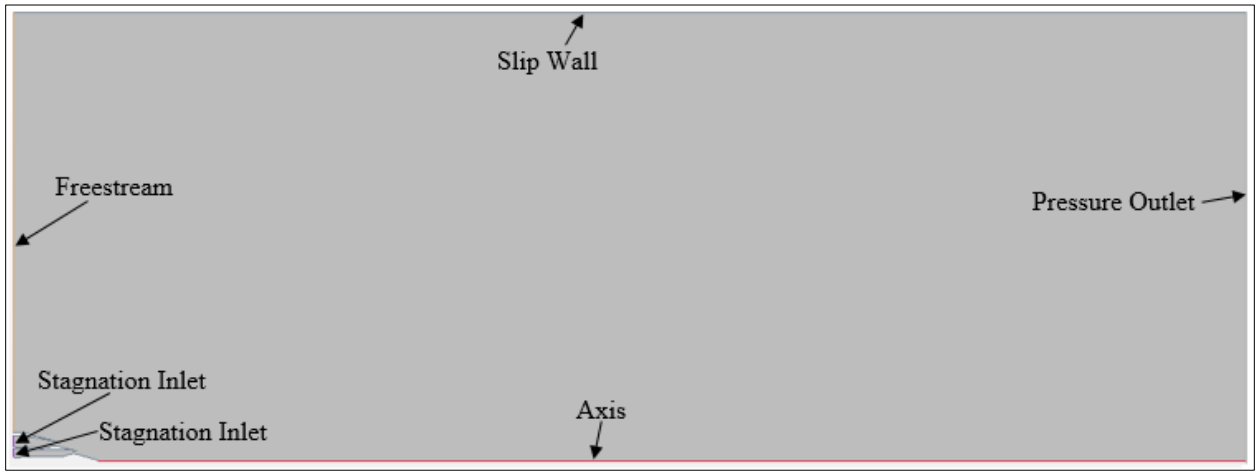

Figure 3.7: Domain with Boundary Conditions for the 3BB Nozzle

3.2.2.3 Chevron Nozzles

Apart from the baseline nozzle, all other nozzles were modeled in 3-D. The trimmer mesher and wall functions were employed here as well. Since the chevrons were symmetric about 30° of the nozzle circumference, a 30° sector of the circumferential segment of the nozzle extending from one end of a chevron to the other, was modeled on STAR-CCM+. In comparison to modeling the entire nozzle with chevrons, this helped to lower the grid size and reduced the overall computational cost. Further, just as in the grid generated for the 3BB nozzle, a wake refinement zone was added in the downstream region of the nozzle to ensure that the flow was fully captured. Since the chevron nozzles were all modeled in similar ways, a close-up of the mesh generated for a 30° sector of only the 3I12I12 nozzle is presented here in Figure 3.8.

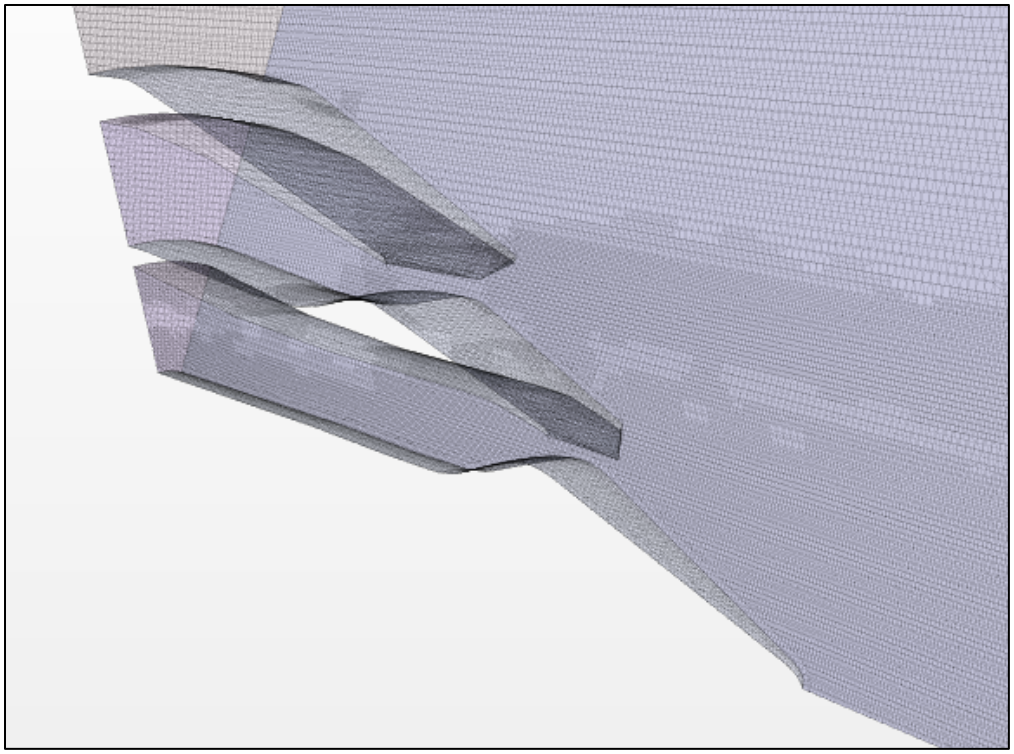

Figure 3.8: Close-Up of 3-D Mesh Generated for the 3I12I12 Nozzle

Table 3.3 outlines the total cell count of the meshes generated for the 3I12I12, $3ITw12_RITw12_L$ and $3ITw12_RITw12_R$ nozzles.

Table 3.3: Total Number of Cells in the Chevron Nozzle Domains

Nozzle	Cell Count (in millions)
3I12I12	5.22
$3ITw12_RITw12_L$	5.24
$3ITw12_RITw12_R$	5.22

The boundary conditions for the domains created for the chevron nozzles were very similar to those used for the baseline nozzle except that no axis was defined here and that the two outer walls of the 30° segment of the domain were modeled as symmetry planes. The domain extended 5.5 fan nozzle exit diameters in the radial direction and 54.3 fan nozzle exit diameters downstream of the external plug tip. Figure 3.9 shows the domain and boundary conditions created for the chevron nozzles.

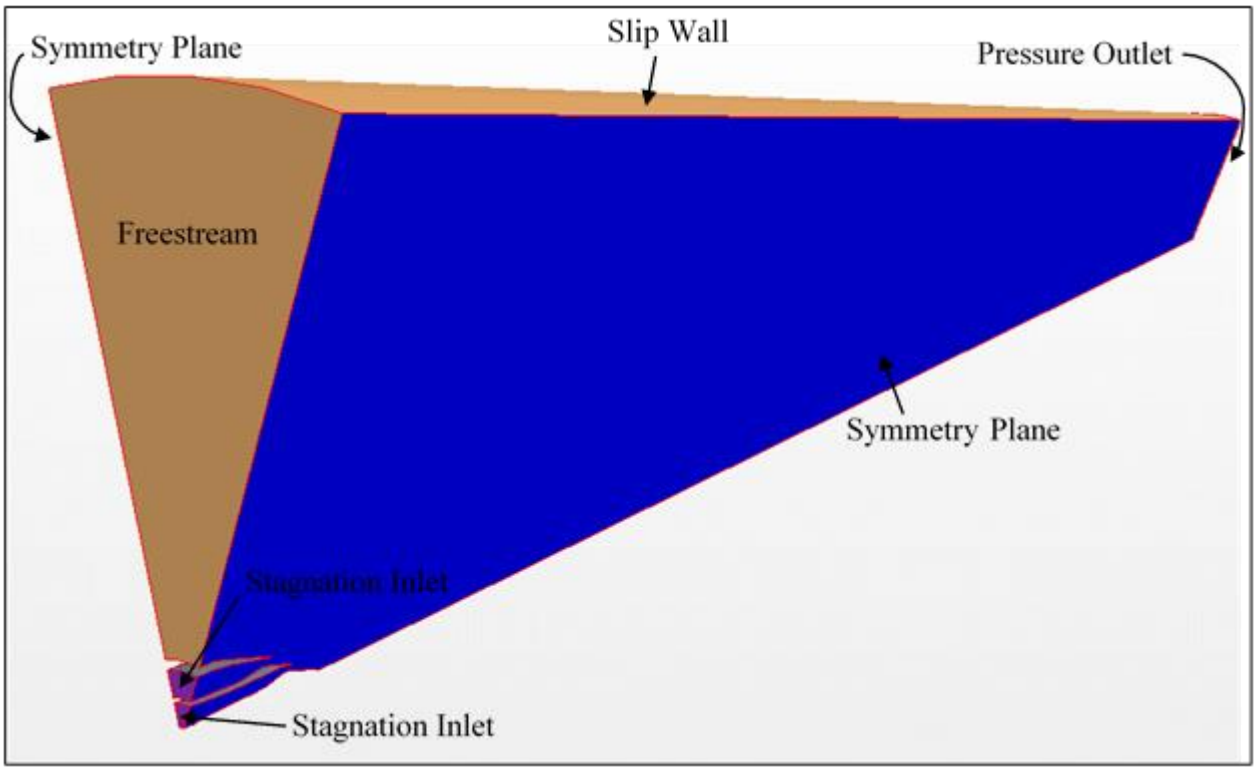

Figure 3.9: Domain with Boundary Conditions for the Chevron Nozzles

3.2.3 Results

In this section, first, the results of the CFD simulations for the baseline nozzle are compared with the PIV results obtained by Bridges and Wernet [24]. Then, a comparative study of centerline parameters for the 3BB nozzle is presented wherein the data obtained here using STAR-CCM+ is compared with that obtained by using the CRAFT [26] and WIND [27] codes. This serves to observe the performance of STAR-CCM+ in analyzing jet flows. Centerline plots of each nozzle considered in the present work are also shown. Since the turbulent kinetic energy has a direct influence on the jet noise, numerical comparisons of the turbulence in the jet structure for each nozzle configuration are presented too. For each nozzle, CFD predicted contours of the TKE levels are first shown on two planes. Following this, TKE contours are also provided at certain axial locations downstream of each nozzle to compare how the turbulence in the flowfield compares from one nozzle to another.

The turbulent kinetic energy is measured at seven axial locations. These locations are measured from the fan nozzle exit plane of the baseline nozzle. At each measuring station, a cross-section

in the YZ plane is used to collect information on the TKE levels. Figure 3.10 shows a schematic of the axial distances at which the jet flow is analyzed.

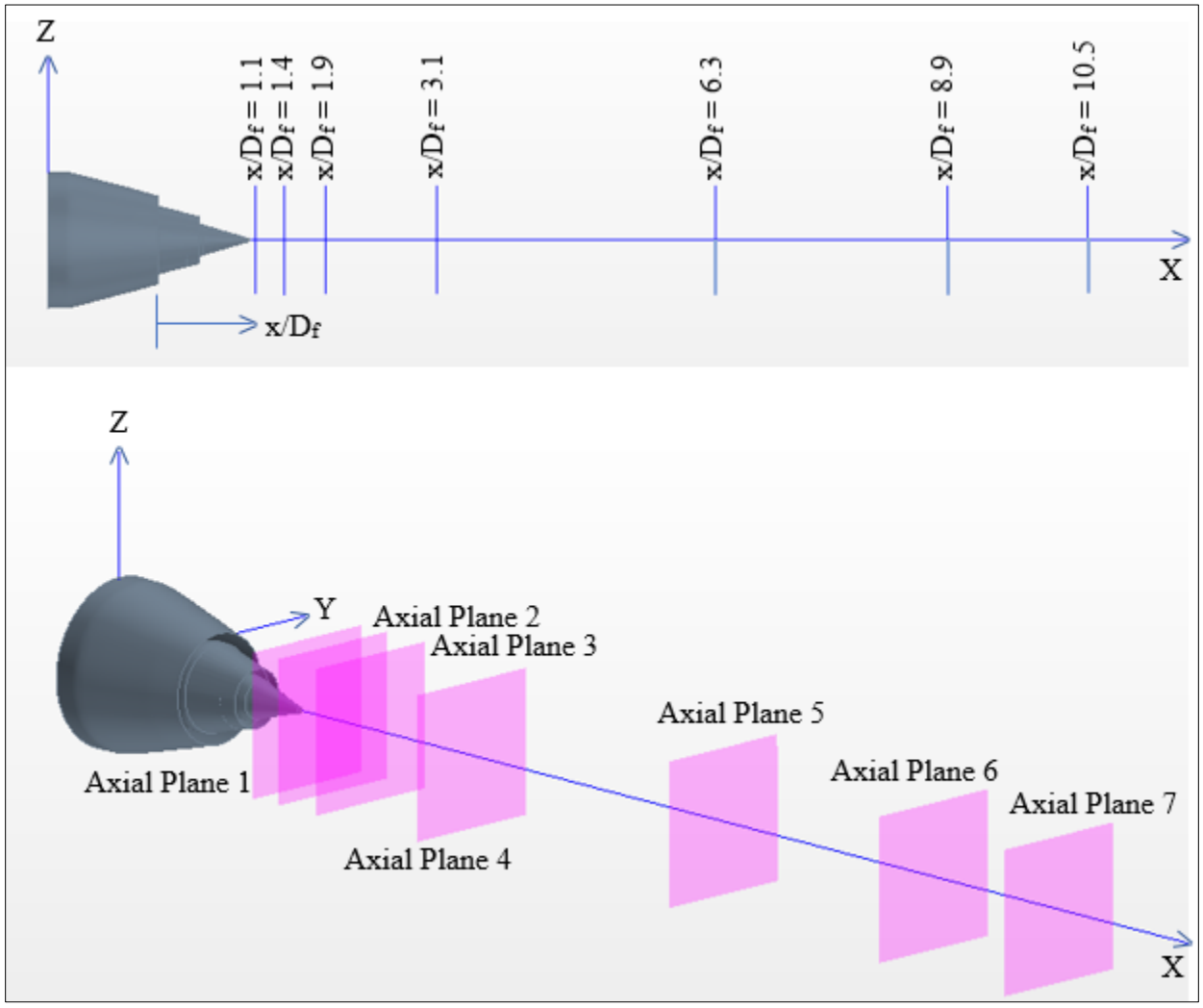

Figure 3.10: Cross-Sectional Scans at Various Axial Distances Downstream of Each Nozzle (Top: Side View, Bottom: Isometric View)

Figure 3.11 shows the mean axial velocity for the 3BB nozzle as reported by Bridges and Wernet [24] using the PIV technique. Figure 3.12 shows the axial velocity for the 3BB model calculated using STAR-CCM+. All velocity and turbulence contours presented here are scaled according to the scale shown in Figure 3.11. The origin in this scale is set at the fan nozzle exit plane.

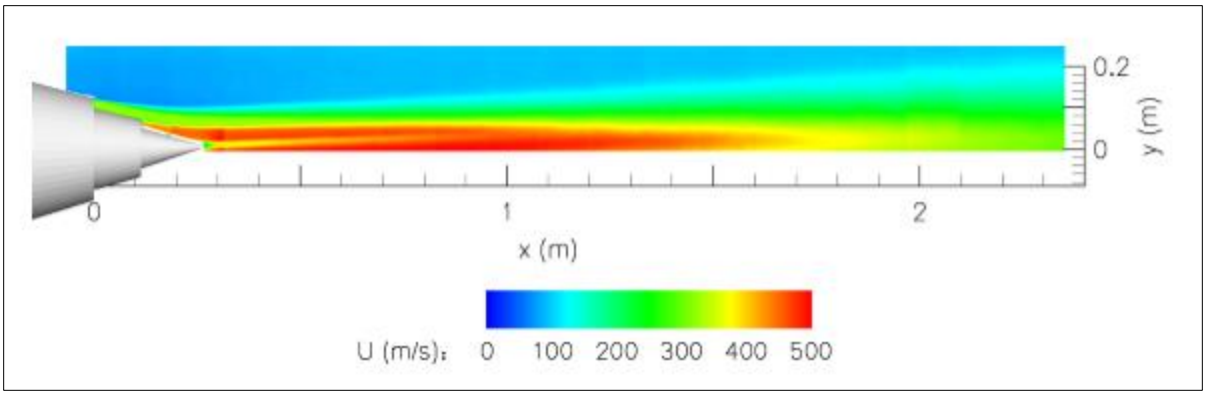

Figure 3.11: Mean Axial Velocity for the 3BB Nozzle using PIV [24]

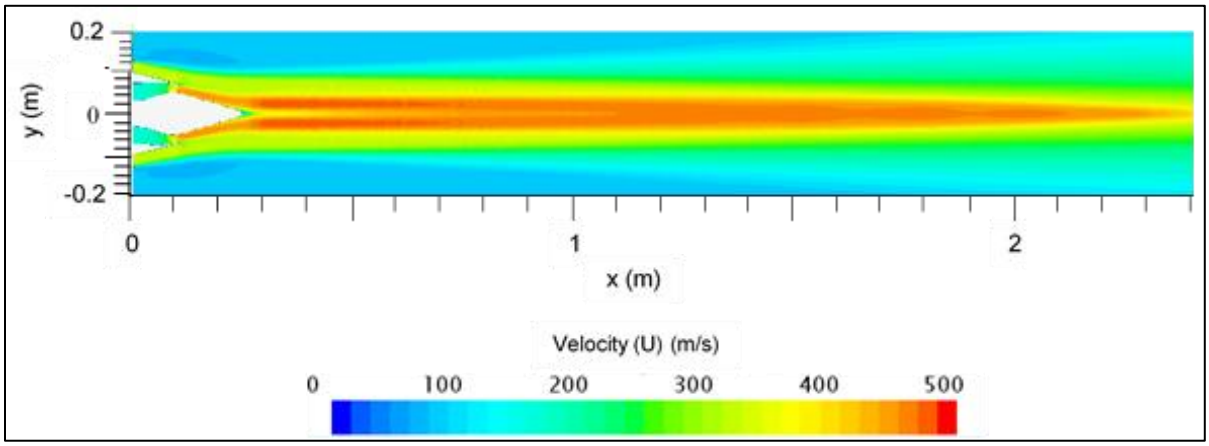

Figure 3.12: Mean Axial Velocity for the 3BB Nozzle using STAR-CCM+

In comparing Figure 3.11 with Figure 3.12, it is observed that both, the PIV results and the CFD analysis, indicate a small recirculation region just downstream of the external plug that is introduced because of the plug's blunt trailing edge. It is also evident that the SST k-ω model overpredicts the length of the potential core of the jet. While the PIV analysis demonstrates that the potential core extends out to about 2 m or so, the numerical analysis shows it to stretch out to about 2.5 m. The axisymmetric flowfield in Figure 3.11 shows the mean axial velocity to peak at about 500 m/s. In contrast, the CFD results slightly underpredict the peak velocity. In general, however, the jet spread is seen to be similar in both images.

Figure 3.13 shows the TKE contours obtained through the use of PIV. The TKE found through CFD is presented in Figure 3.14.

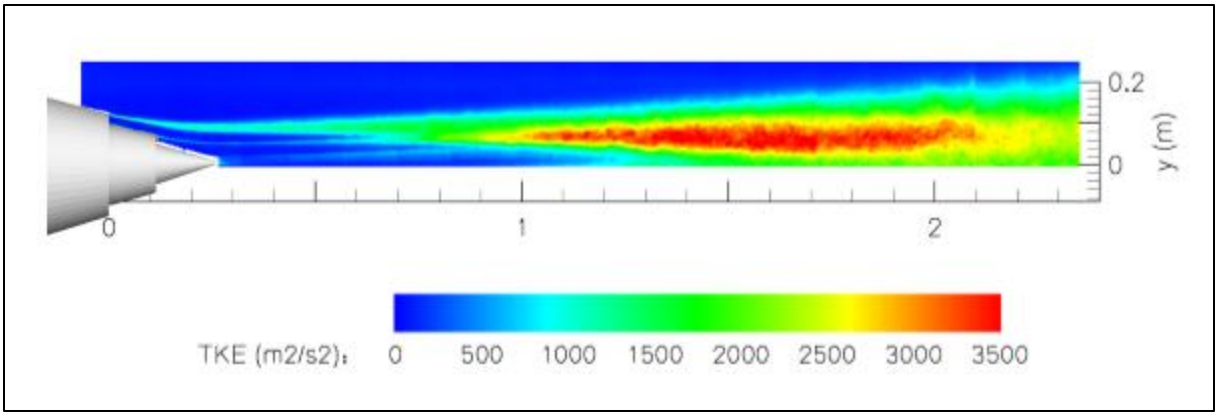

Figure 3.13: Turbulent Kinetic Energy for the 3BB Nozzle using PIV [24]

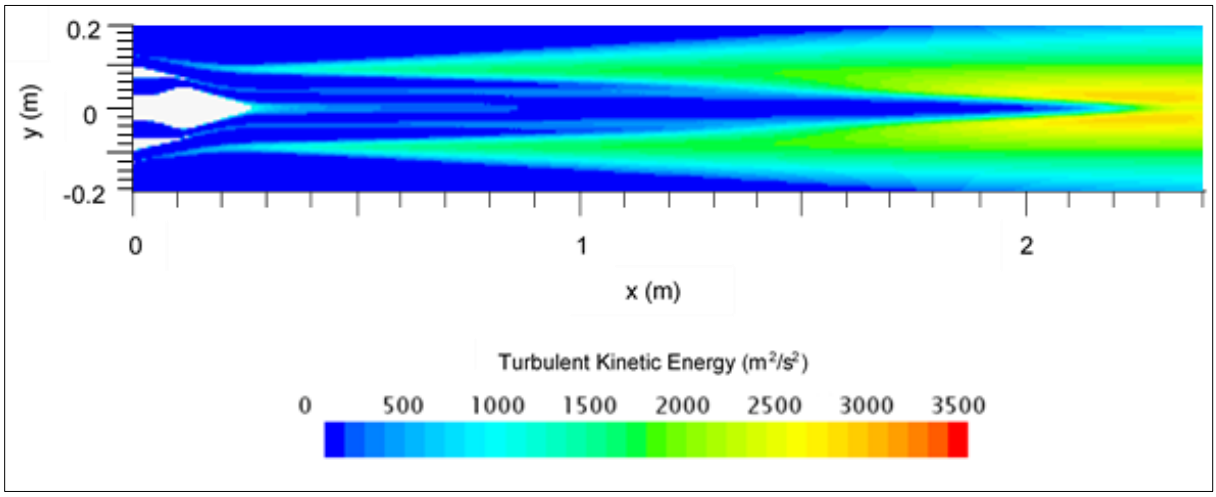

Figure 3.14: Turbulent Kinetic Energy for the 3BB Nozzle using STAR-CCM+

The turbulent kinetic energy captured through PIV in Figure 3.13 shows peak TKE levels at approximately 3500 m^2/s^2 between 1 m and 2.1 m downstream of the fan nozzle exit. In contrast, the SST k-ω turbulence model underpredicts the amount of turbulent kinetic energy produced. The results from STAR-CCM+ show that the TKE peaks at about 2830 m^2/s^2 and is observed further downstream of the fan exit. However, both images show that high TKE levels are experienced in the jet mixing region. Further, as has been reported earlier in the literature review, it is noticeable that weak mixing occurs between the fan and core shear layers and that the turbulence in the jet is dominated by the mixing of the fan and freestream shear layers. As far as the TKE is concerned, similar results are presented by Kenzakowski et al [26] through the use of the CRAFT code. For the baseline 3BB nozzle, in comparison to the peak TKE value of about 2830 m^2/s^2 calculated here using STAR-CCM+, Kenzakowski used the k-ε turbulence model and observed that the TKE peaked at approximately 2700 m^2/s^2.

Figure 3.15 lays out a plot showing the relationship between the centerline velocity and the axial distance for the 3BB nozzle. The graph compares the data obtained from STAR-CCM+ with that available from the literature review. The axial distance on the plot is normalized with respect to the fan nozzle exit diameter (D_f) which is measured to be about 9.55 in.

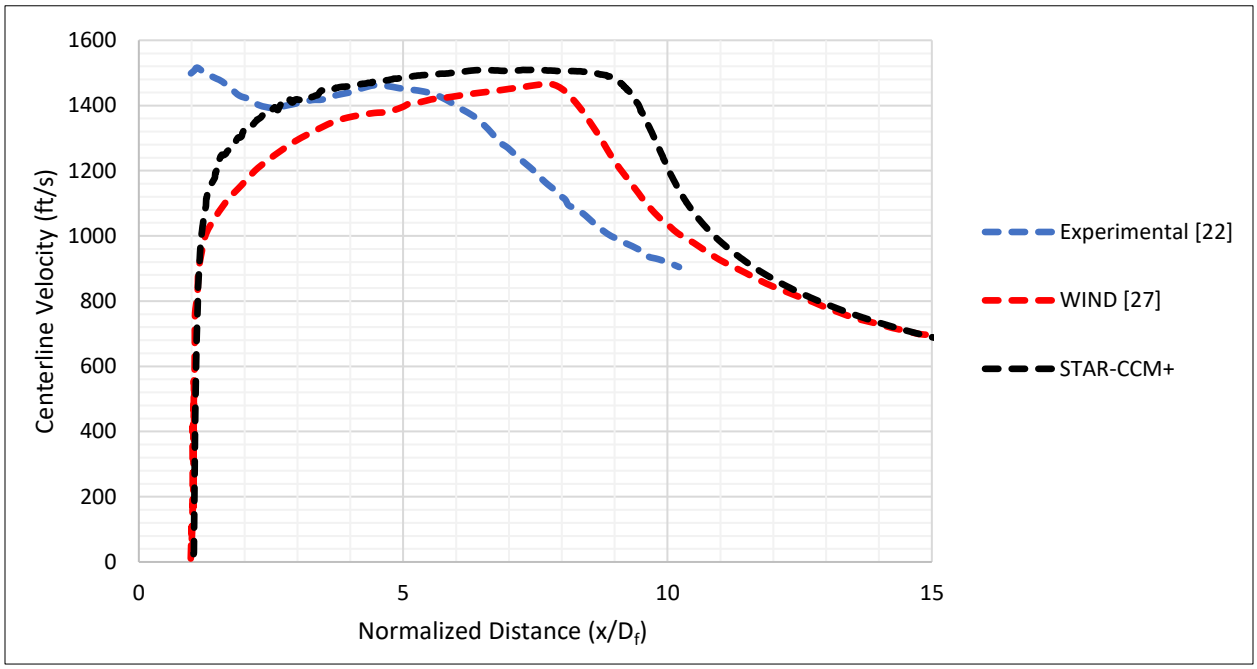

Figure 3.15: Variation of Centerline Velocity with the Normalized Axial Distance for the 3BB Nozzle

The potential core of a jet is characterized by a constant velocity profile. Beyond the potential core, the velocity of the flow gradually diminishes as the flow transitions from the potential core region to the mixing region. In the plot shown above in Figure 3.15, the decline in the centerline velocity curves is clearly indicative of the end of the potential core. Here, it is observed that the SST k-ω turbulence model in STAR-CCM+ is able to correctly show the trend of the centerline velocity of the exhaust jet. However, it suffers from the problem of overpredicting the length of the potential core. While the results from the WIND code presented by Koch et al [27] come closer to the experimental data in predicting the potential core length, they still fall short of matching up closely. In that regard, the data obtained from STAR-CCM+ is able to overlap with some of the experimentally available results. Overall, the trend of the experimental results, and the results obtained from the WIND code and STAR-CCM+ seem to converge at about 13 fan diameters downstream of the nozzle.

Figure 3.16 shows a graph of the centerline total temperature as a function of the normalized axial distance for the 3BB nozzle.

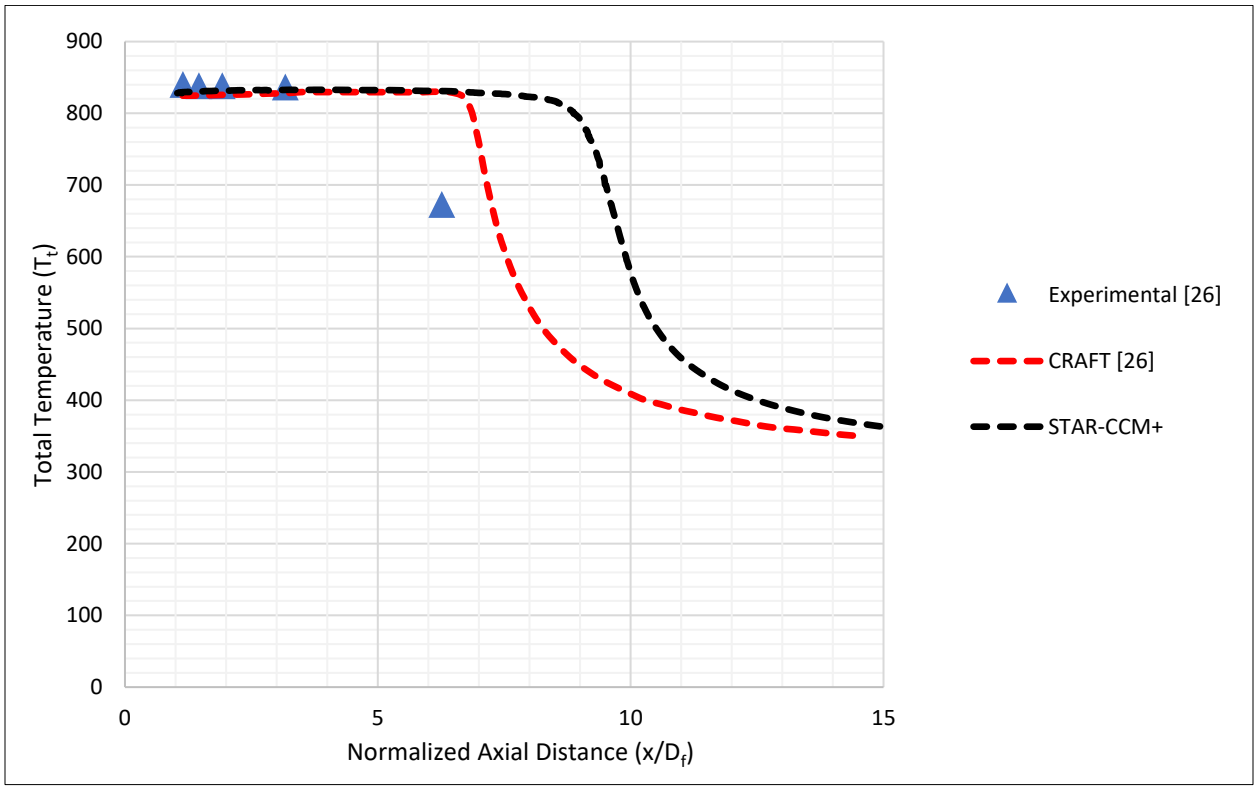

Figure 3.16: Variation of Centerline Total Temperature with the Normalized Axial Distance for the 3BB Nozzle

The theory of turbulent jets shows that the temperature of the fluid in the potential core region is constant and equal to the temperature of the jet exiting the nozzle [38]. Further, since the velocity in this region is constant too, it can be inferred that the stagnation temperature also remains constant here. As a result, just like the centerline velocity, plotting the total temperature against the axial distance downstream of the nozzle also gives an idea of the extent to which the potential core extends. Hence, the conclusions that can be drawn by looking at Figure 3.16 are similar to those obtained from Figure 3.15. However, in comparison to the centerline velocity data, a better overlap between the experimental results and those obtained from the WIND code and STAR-CCM+ is observed.

Figure 3.15 shows that in comparison to the data obtained through experimental methods, the results from WIND and STAR-CCM+ show an overprediction of the potential core while showing similar trends. In this regard, it is necessary to explore the behavior of these curves after

the potential core ends. For this purpose, a comparison of the rates of decline of the centerline velocities is carried out. To achieve this, first, a section is selected on each curve between the same y-intercepts where the curve is assumed to be almost linear. Here, all three curves are assumed to be linear between 1000 ft/s and 1400 ft/s. Following this, the respective x/D_f values are read for each selected section corresponding to the two y-intercepts. Once these points are retrieved, the slopes are calculated and compared. Table 3.4 shows the calculated values of the slopes for the three data sets.

Table 3.4: Comparison of the Rates of Decay of the Centerline Velocity between the Experimental [22], WIND [27] and STAR-CCM+ Data

	Experimental	WIND	STAR-CCM+
Slope, $\frac{dU}{d(x/D_f)}$ (ft/s)	133.3	216.2	250

It is observed that the two CFD approaches show a faster rate of decline of the centerline velocity. While the rates come relatively close between the numerical methods, STAR-CCM+ shows the steepest rate of decrease. The experimental results show a gradual, more relaxed decline in the centerline velocity.

To further explore the post-potential core region, an error analysis is carried out for the three curves in Figure 3.15 to observe how the WIND and STAR-CCM+ codes overshoot the length of the potential core as seen experimentally. The experimental results show that the centerline velocity reaches a peak velocity of slightly over 1440 ft/s before declining till about 900 ft/s. Using centerline velocity values between 1440 ft/s and 900 ft/s, the corresponding x/D_f values are read for each of the three data sets. Clearly, since the numerical methods overpredict the experimental potential core region, a difference exists between the normalized distance for each velocity point in the chosen range between the numerical methods and the experimental results. This difference in the normalized distance then becomes the basis of the error analysis presented here. Figure 3.17 shows the errors observed.

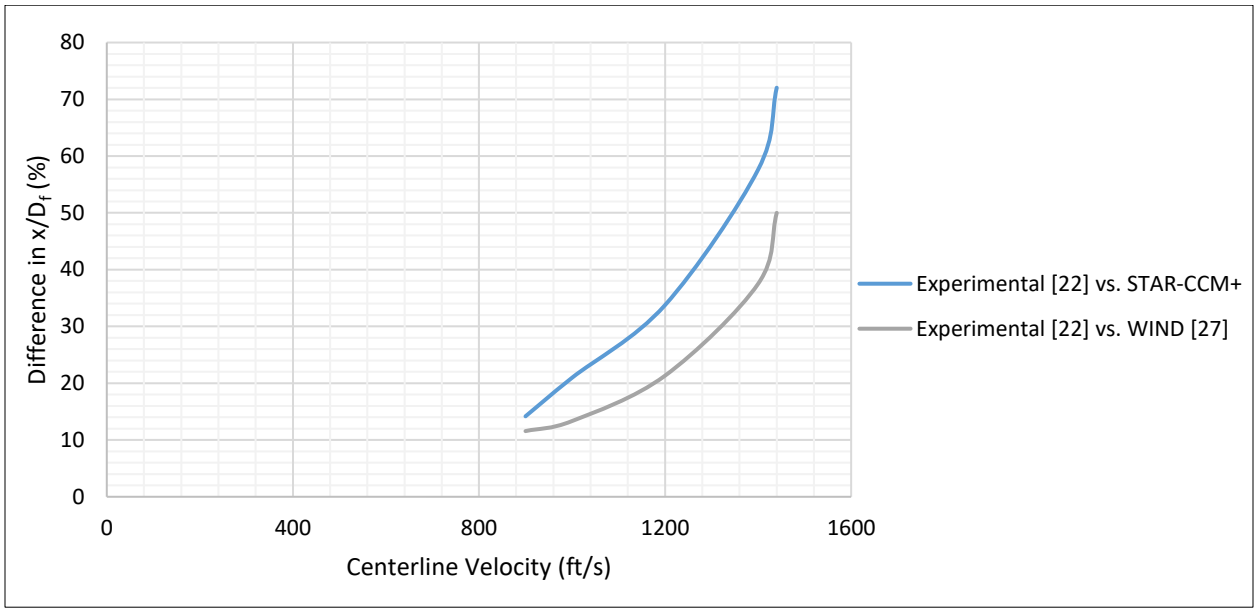

Figure 3.17: Differences in the Normalized Axial Distances between the Computational and Experimental Data Corresponding to Centerline Velocities in the Post-Potential Core Region

Before the end of the potential core, the data from STAR-CCM+ overlapped with some of the results obtained experimentally approximately between $x/D_f = 2.5$ and $x/D_f = 5$, while the results from the WIND code failed to match up with any of the experimental results in this region. However, as is seen in the graph above, beyond the potential core, the WIND code does a better job at approximating the x/D_f location for each respective centerline velocity value as compared to the data obtained from STAR-CCM+. In comparison to the experimental results, for both numerical methods, a decrease is observed in the x/D_f location as the value of the centerline velocity decreases beyond the potential core region. At 1440 ft/s, when the centerline velocity is starting to fall at about $x/D_f = 5$ for the experimental data, the WIND and STAR-CCM+ codes show the highest offshoot in the normalized distance for this velocity. For STAR-CCM+, the normalized distance corresponding to a centerline velocity of 1440 ft/s in the post-potential core region overshoots the experimental normalized distance by 72% whereas that difference is 50% in case of the WIND code. As the centerline velocity falls, the error in the x/D_f location recorded experimentally gradually drops too. At about 900 ft/s, compared to the experimental results, the error in the x/D_f location recorded through STAR-CCM+ is about 14% while the WIND data shows an error of about 12%. Going by the trends demonstrated by the curves in Figure 3.15, it

can be inferred that the mismatch in the recorded axial locations between the three sources continues to diminish as the centerline velocity falls with increasing distance downstream.

A similar analysis as the one described above is carried out for the data presented in Figure 3.16. As is visible in Figure 3.16, the results from the CRAFT solver and STAR-CCM+ make up reasonable data sets. In the absence of enough data points for the experimental results in this case, the rate of decline of the centerline T_t is calculated for the two computational methods. For this purpose, it is assumed that the CRAFT and STAR-CCM+ data showcase linear characteristics between 700 K and 500 K. These now become the y-intercepts to be used for the calculations of the slopes for each curve.

Table 3.5 shows the calculated rates of decline of the centerline total temperature from CRAFT and STAR-CCM+.

Table 3.5: Comparison of the Rates of Decay of the Centerline Total Temperature between the CRAFT [26] and STAR-CCM+ Data

	CRAFT	STAR-CCM+
Slope, $\frac{dT_t}{d(x/D_f)}$ (K)	200	201.4

It is observed that after the potential core ends, the results from CRAFT and STAR-CCM+ show almost the same rate of decline in the centerline total temperature. Since no experimental data points exist showing how the centerline total temperature declines after the potential core ends, no conclusions can be drawn here about how the rates calculated numerically compare with the experimental rate of decline.

The error analysis presented in case of the centerline velocity and described earlier, is performed for the centerline total temperature data too. The error calculations are performed for various total temperature values lying between 800 K and 350 K, with the latter value point being the last data point in the CRAFT data set. Figure 3.18 presents the errors in the normalized distances against the centerline total temperatures between the two numerical approaches.

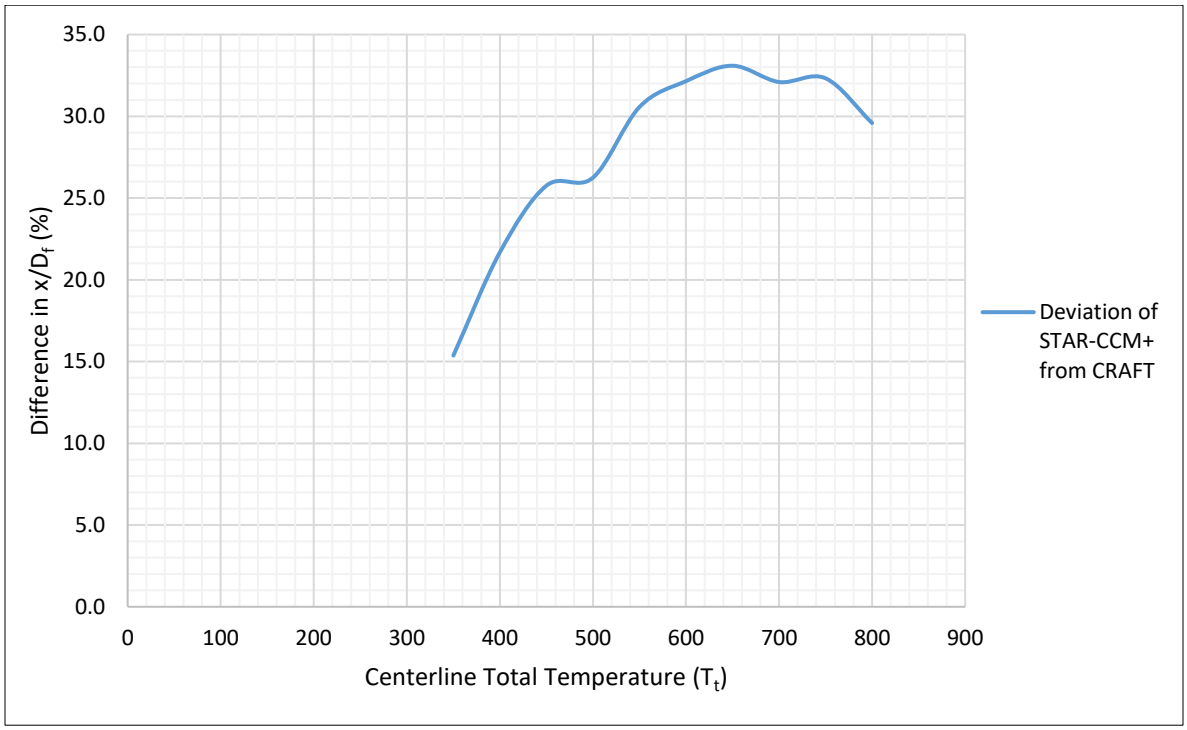

Figure 3.18: Differences in the Normalized Axial Distances between the CRAFT [26] and STAR-CCM+ Data Corresponding to Centerline Total Temperatures in the Post-Potential Core Region

It is observed that the difference in the normalized location corresponding to a certain total temperature value gradually decreases as the total temperature declines after the end of the potential core. However, interestingly, this gradual decrease in the x/D_f error comes after a maximum error at about 650 K. Initially, at 800 K, the error in the normalized distance between the CRAFT and STAR-CCM+ results lies at about 30%. A peak in the error is seen at 650 K with it being about 33%. As the total temperature drops below 650 K, the errors gradually decrease. At 350 K, the lowest difference in the x/D_f values is observed between the two codes and is recorded to be approximately 15%.

The numerical analysis of the 3BB nozzle carried out in STAR-CCM+ is now used as a reference for comparison with the chevron nozzles presented in this work. As mentioned earlier for the 3BB nozzle, centerline parameters are considered for the chevron nozzles too. Figure 3.19 shows a plot of the centerline velocity with respect to the normalized axial distance for each nozzle while Figure 3.20 presents a graph displaying the centerline total temperature distribution with the distance downstream.

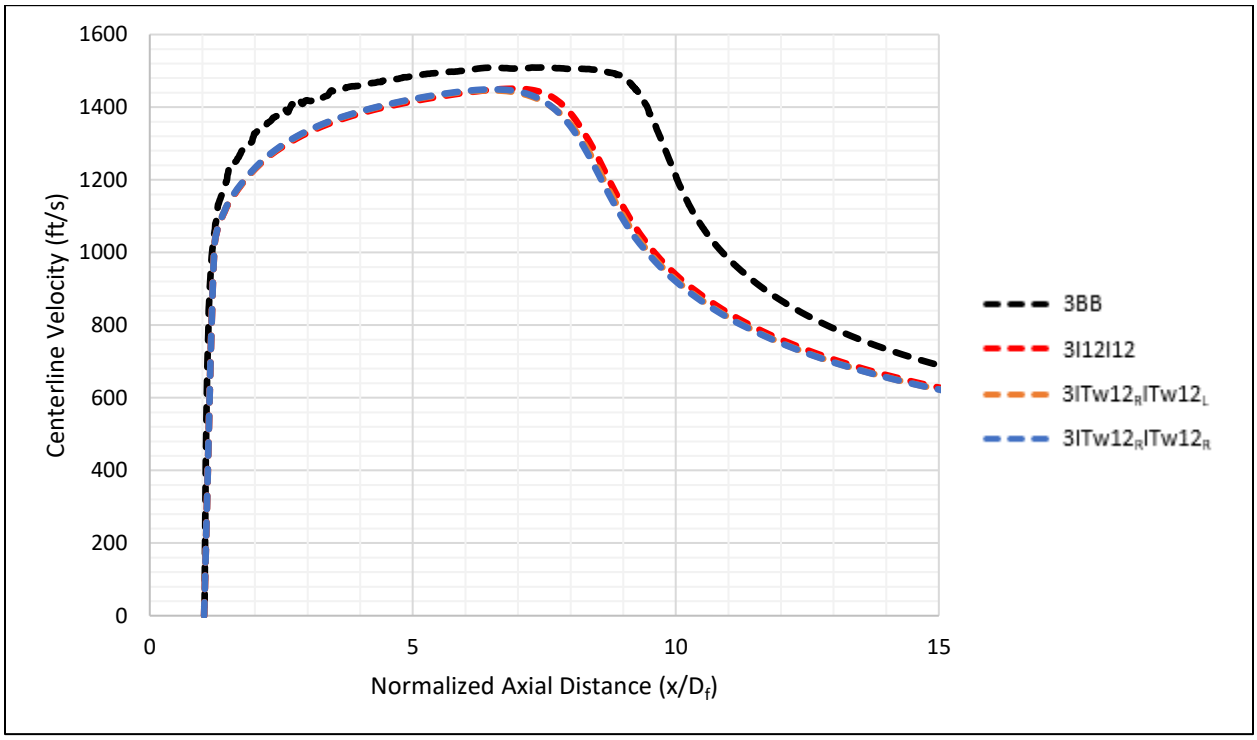

Figure 3.19: Variation of Centerline Velocity with the Normalized Axial Distance for the Baseline and Chevron Nozzles

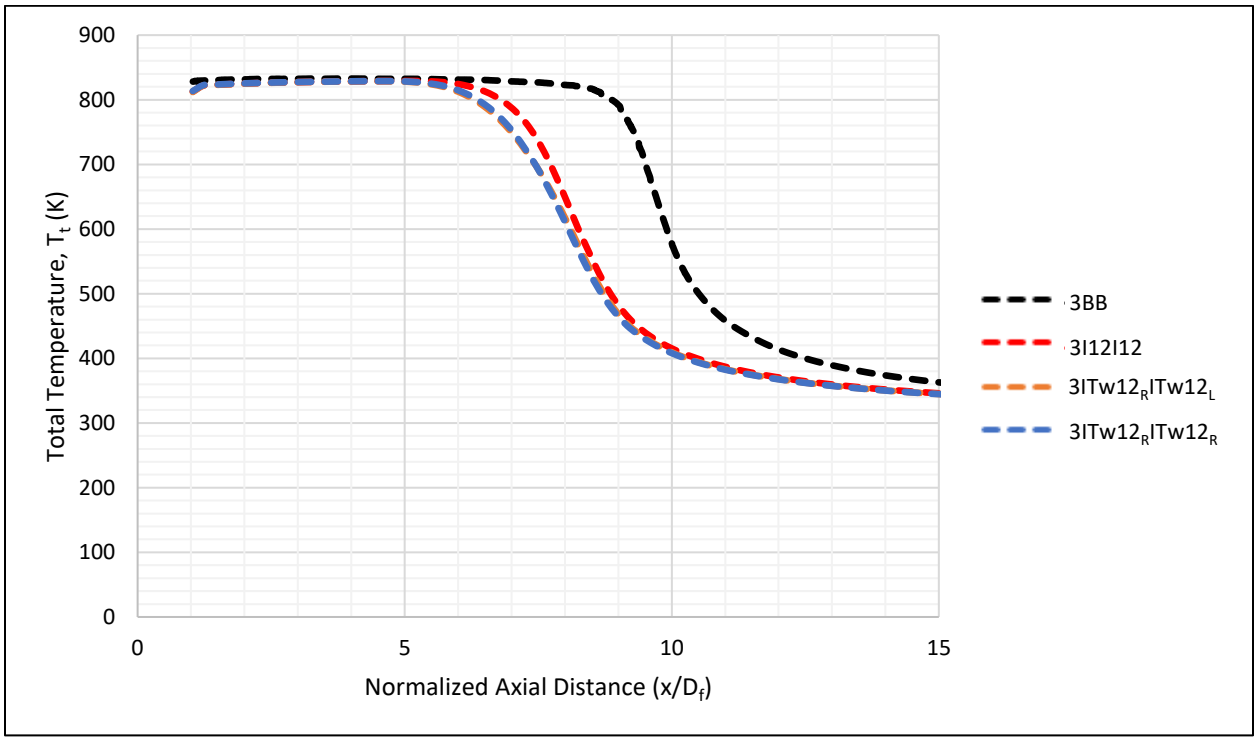

Figure 3.20: Variation of Centerline Total Temperature with the Normalized Axial Distance for the Baseline and Chevron Nozzles

The effect of the chevrons is clearly visible in the two plots shown above. For the 3BB nozzle, the potential core extends till about 9 fan diameters downstream of the nozzle. In contrast, the chevron nozzles considered here show a potential core that extends to about 7 fan diameters. Interestingly, the chevron nozzles demonstrate almost identical behaviors with very subtle differences existing between the 3I12I12, $3ITw12_{R}ITw12_{L}$ and $3ITw12_{R}ITw12_{R}$ models. However, a close inspection of the data suggests that the $3ITw12_{R}ITw12_{R}$ nozzle shows the smallest potential core with the lowest centerline velocity distribution in comparison to the other two chevron nozzles.

To better compare the jet flow from the nozzles and to visualize how the chevrons alter the jet, the flowfield from each nozzle is observed on two azimuthal planes – one passing through the chevron tip (0° azimuthal plane) and the other through the valley (15° azimuthal plane). Figure 3.21 and Figure 3.22 show the velocity and TKE contours, respectively, on the 0° azimuthal plane while Figure 3.23 and Figure 3.24 present the same contours, respectively, through the 15° azimuthal plane. The origin in each graph is set at the fan nozzle exit plane of the baseline nozzle.

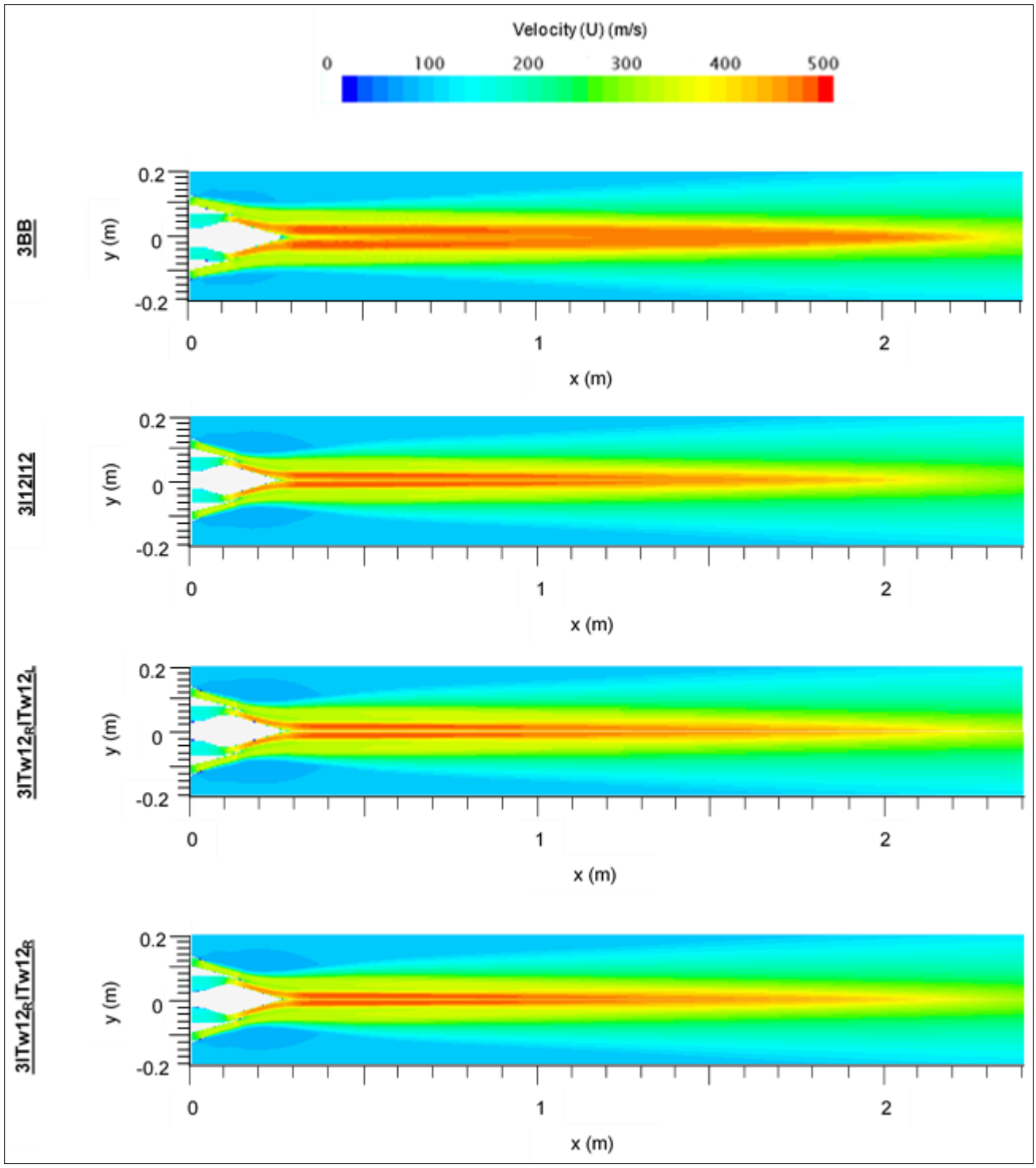

Figure 3.21: Velocity Contours of Each Nozzle on the 0° Azimuthal Plane

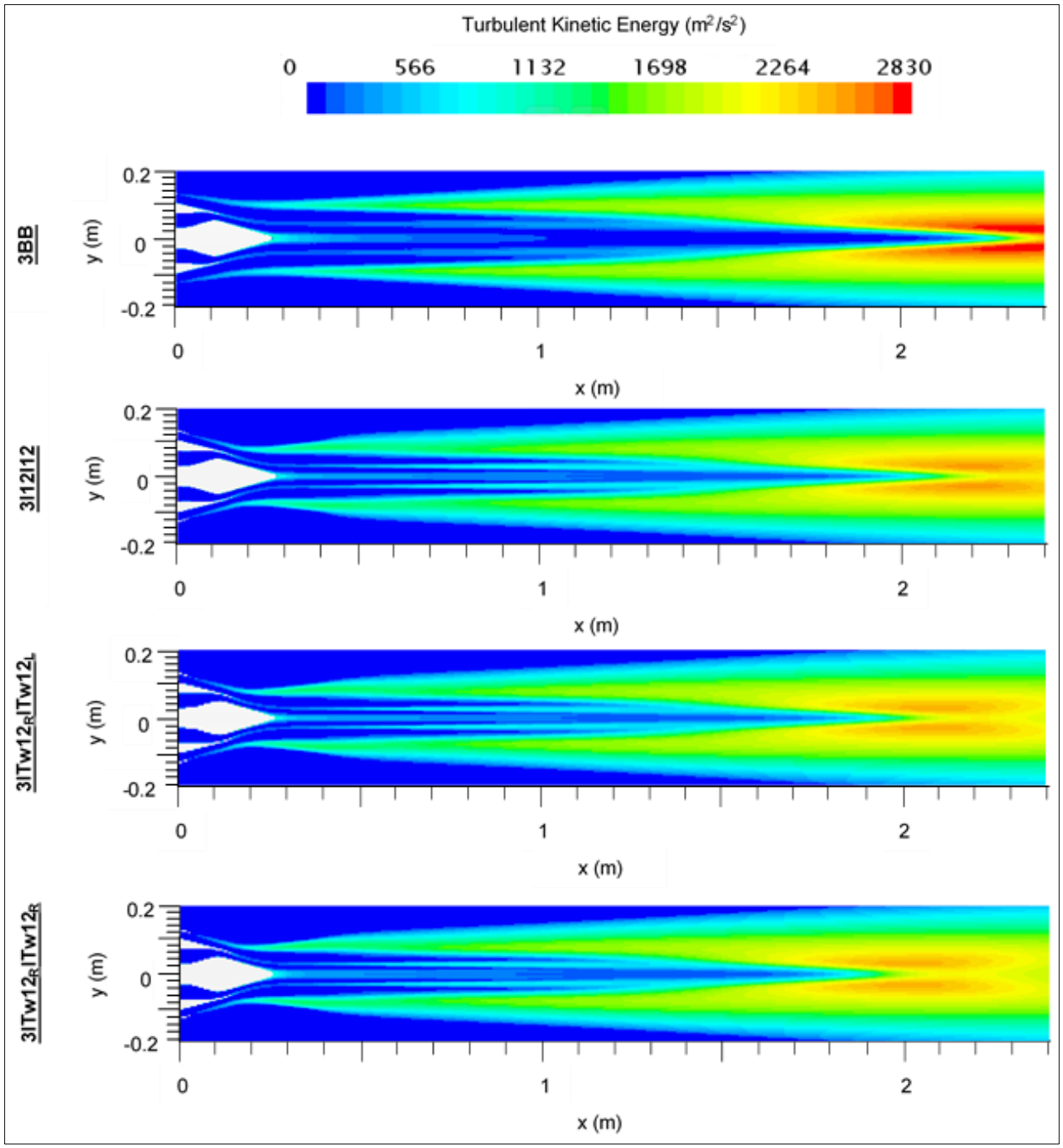

Figure 3.22: TKE Contours of Each Nozzle on the 0° Azimuthal Plane

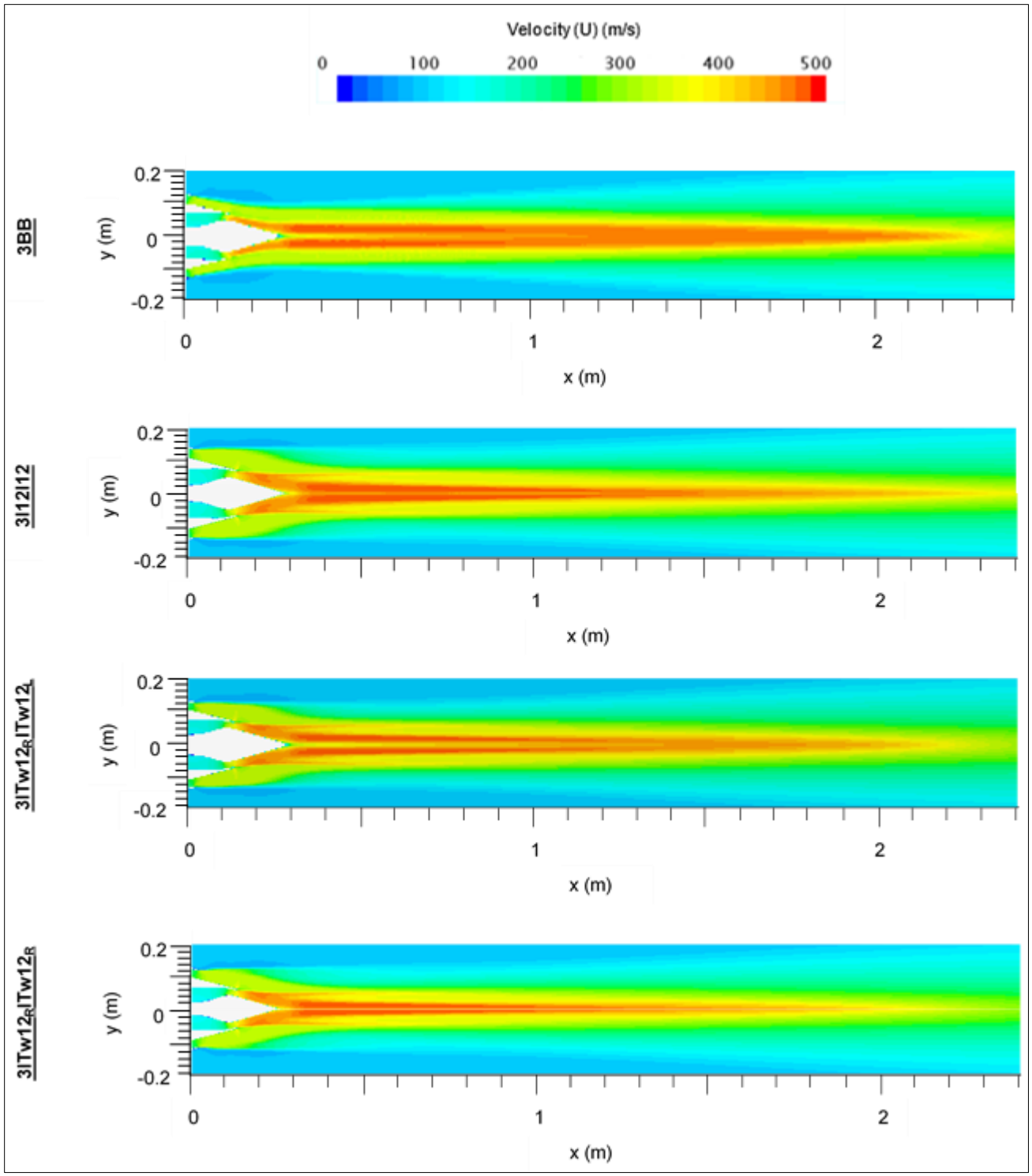

Figure 3.23: Velocity Contours of Each Nozzle on the 15° Azimuthal Plane

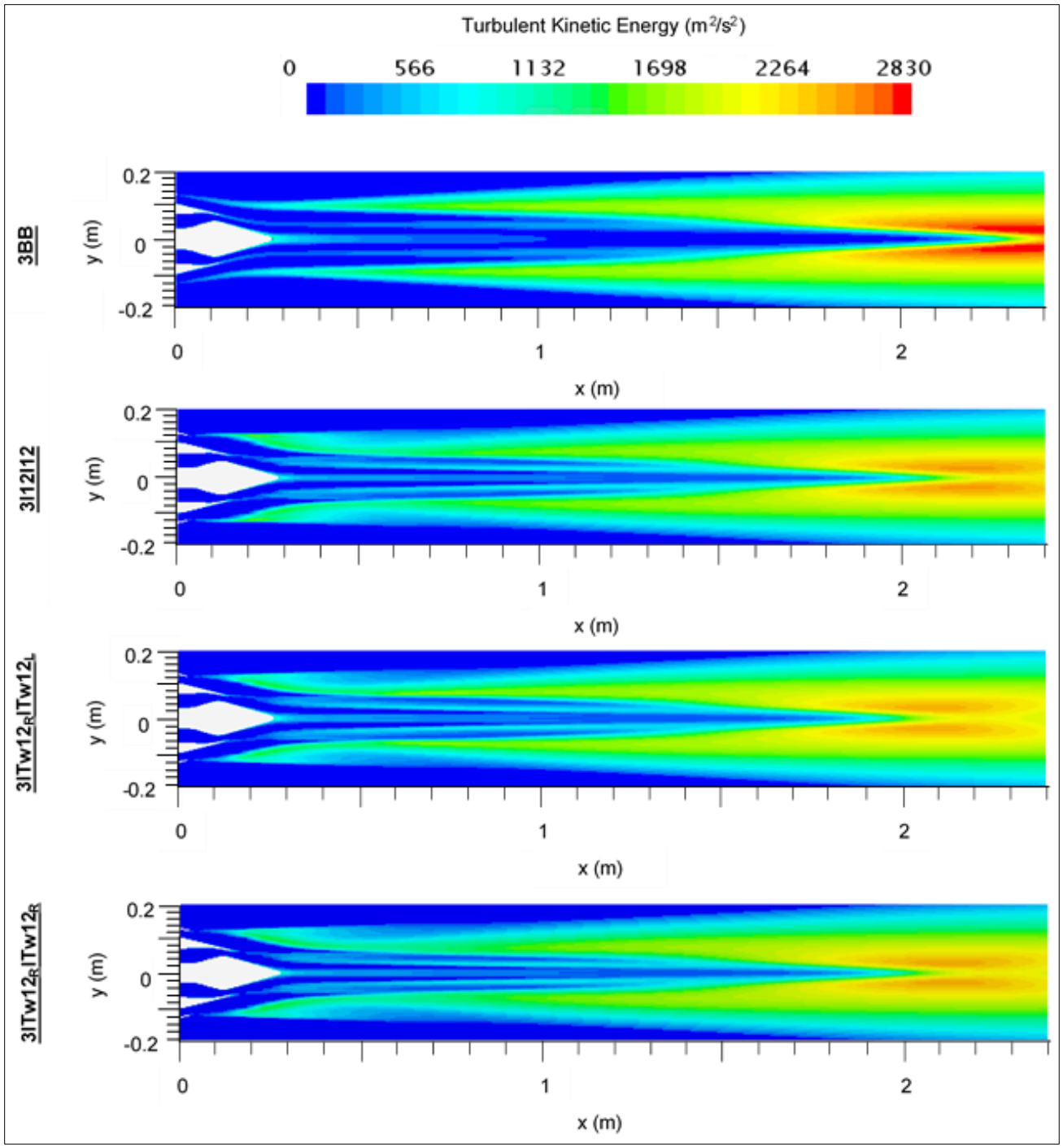

Figure 3.24: TKE Contours of Each Nozzle on the 15° Azimuthal Plane

Figure 3.21 and Figure 3.23 clearly indicate a shortening of the potential core for the chevron nozzles. The potential core for the 3BB nozzle extends well beyond 2 m. in the scale used. In comparison, the potential core is much shorter for all three chevron nozzles with some differences arising between the two planes in consideration. The 0° azimuthal plane shows the

potential core to extend to about 2 m. for the 3I12I12 and 3ITw12$_R$ITw12$_R$ nozzles while a slightly longer potential core is observed for the 3ITw12$_R$ITw12$_L$ nozzle. However, on the 15° azimuthal plane, the 3I12I12 nozzle shows the longest potential core while the shortest potential core is observed for the 3ITw12$_R$ITw12$_R$ nozzle. An interesting observation is made regarding the width of the potential core in this regard. Compared to the 3BB nozzle, the chevron nozzles show a distinct reduction in the mean width of the potential core. This is due to the inward bend of the chevrons forcing the exhaust jet to flow towards the nozzle centerline more rapidly. In general, when compared to the 3BB nozzle, the chevron nozzles exhibit lower mean axial velocities with the lowest mean axial velocity being observed for the 3ITw12$_R$ITw12$_R$ nozzle.

The turbulence in the jet plume of each nozzle shown in Figure 3.22 and Figure 3.24 demonstrates the extent of mixing in the flows. For each nozzle, the peak in the turbulent kinetic energy is observed slightly off-axis at a certain axial distance downstream before which a gradual decay is seen as the fan and freestream mixing layers reach the centerline. However, it is evident that the chevrons significantly reduce the amount of turbulent kinetic energy in comparison to the amount generated by the baseline nozzle. In case of the 3BB nozzle, the peak in the turbulent kinetic energy is observed beyond 2 m. downstream. In contrast, the peak in the TKE levels is observed further upstream for the chevron nozzles on both azimuthal planes. Both, the 3ITw12$_R$ITw12$_L$ and 3ITw12$_R$ITw12$_R$ nozzles, show a slight reduction in the turbulent kinetic energy compared to what is seen in case of the 3I12I12 nozzle. While the 3I12I12 model shows a peak TKE of 2514 m^2/s^2, the 3ITw12$_R$ITw12$_L$ and 3ITw12$_R$ITw12$_R$ nozzles register 2445 m^2/s^2 and 2446 m^2/s^2 as the highest levels of their TKE, respectively. In relative terms, this translates to the 3I12I12 nozzle showing a reduction of about 11% in the peak TKE value compared to the 3BB nozzle while the 3ITw12$_R$ITw12$_L$ and 3ITw12$_R$ITw12$_R$ nozzles, both, show a reduction of about 14%. In this regard, an interesting observation is made regarding the distances over which the greatest amounts of turbulent kinetic energy are observed. The 3I12I12 nozzle displays the longest extent over which high TKE levels are observed while the plume field of the 3ITw12$_R$ITw12$_R$ nozzle is characterized by the highest amounts of the TKE being confined to the smallest region. The 15° azimuthal plane also shows localized regions just downstream of the chevrons where the TKE levels are high. It is evident that these turbulent areas are not formed as a result of the mixing between the core and fan shear layers. In fact, these turbulent regions are generated by the recirculation zones that exist in the vicinity of the

chevrons. Another indication that these high turbulence regions are not due to the core and fan shear layers mixing with each other is the eventual decay in the TKE values just downstream of these areas.

In order to gain more insight into how the chevrons alter the jet plume, the following figures present a comparative analysis of the turbulent kinetic energy produced for each chevron nozzle at various axial locations downstream measured using the 3BB nozzle's fan exit diameter (D_f) as the reference length.

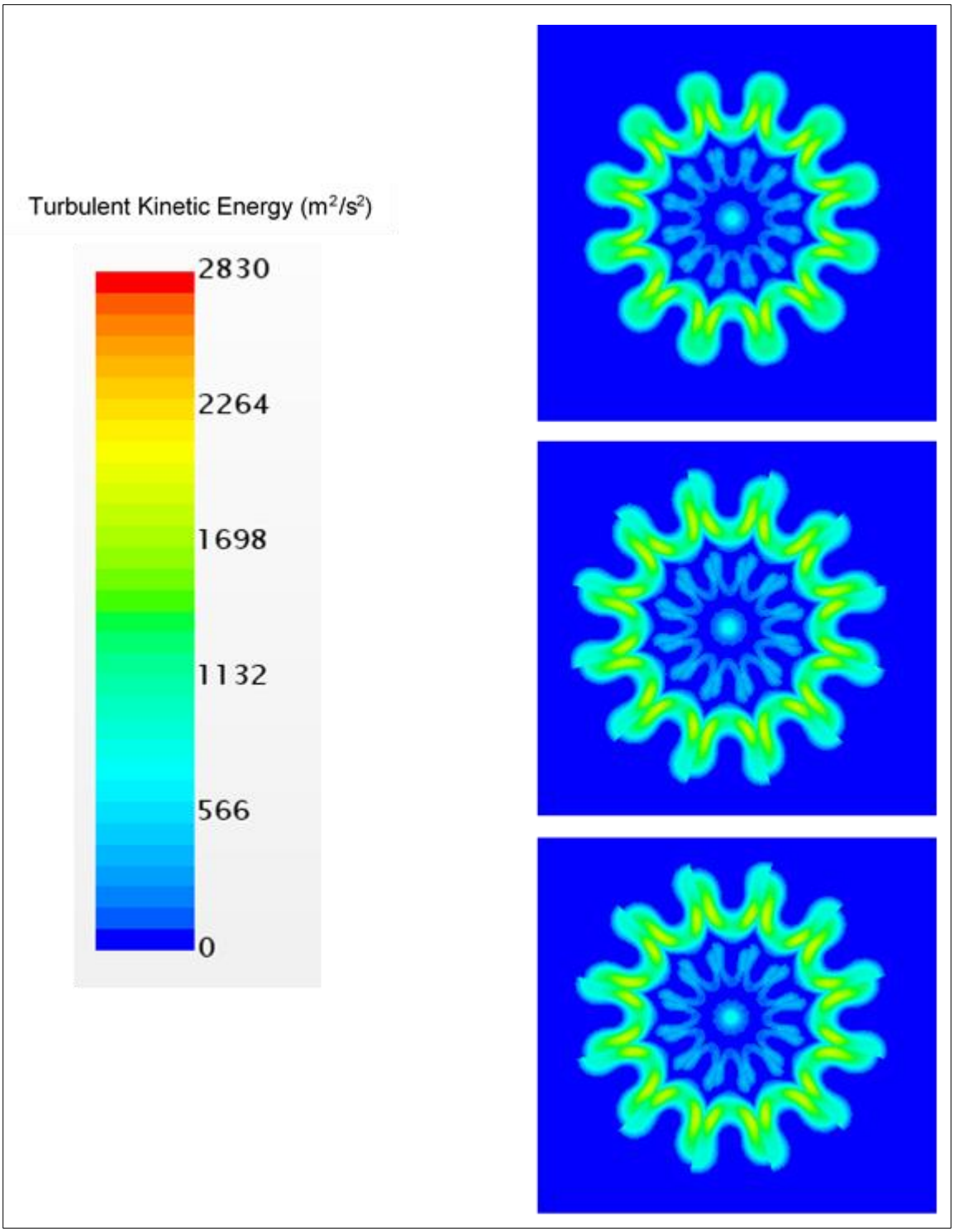

Figure 3.25: Turbulent Kinetic Energy from the Chevron Nozzles at 1.1D_f Downstream (Top: 3I12I12, Middle: 3ITw12$_R$ITw12$_L$, Bottom: 3ITw12$_R$ITw12$_R$)

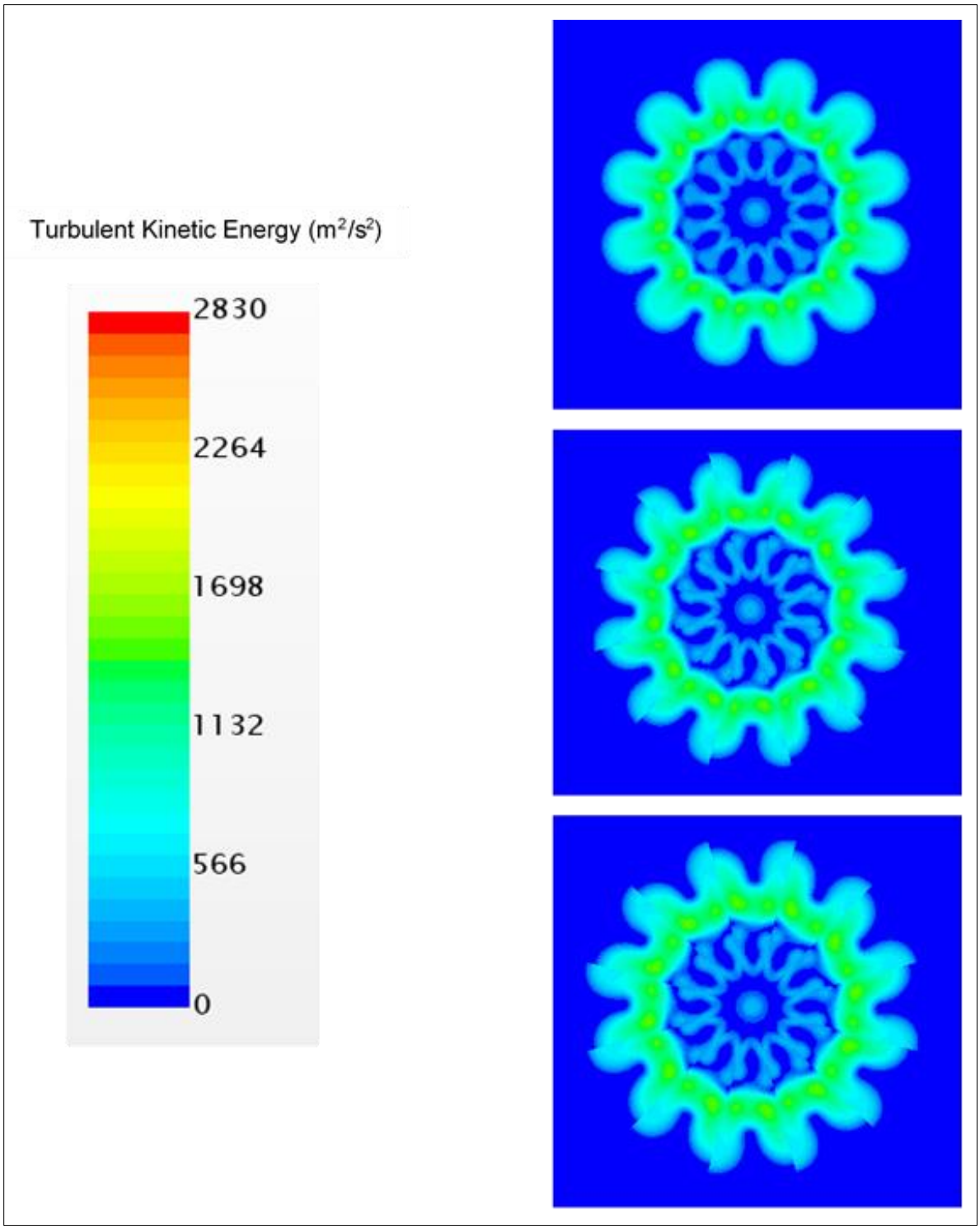

Figure 3.26: Turbulent Kinetic Energy from the Chevron Nozzles at 1.4D_f Downstream (Top: 3I12I12, Middle: 3ITw12$_R$ITw12$_L$, Bottom: 3ITw12$_R$ITw12$_R$)

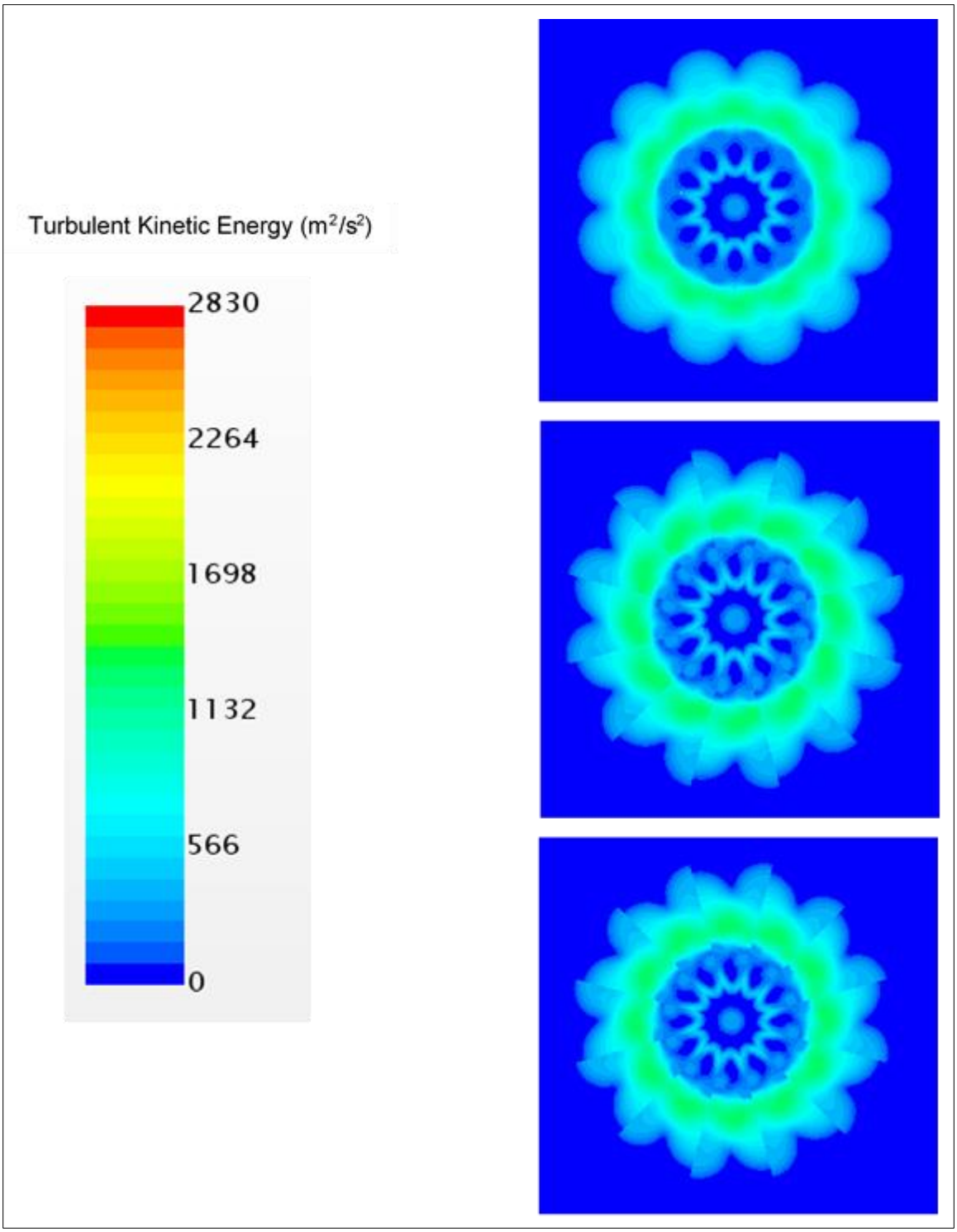

Figure 3.27: Turbulent Kinetic Energy from the Chevron Nozzles at 1.9D_f Downstream (Top: 3I12I12, Middle: 3ITw12$_R$ITw12$_L$, Bottom: 3ITw12$_R$ITw12$_R$)

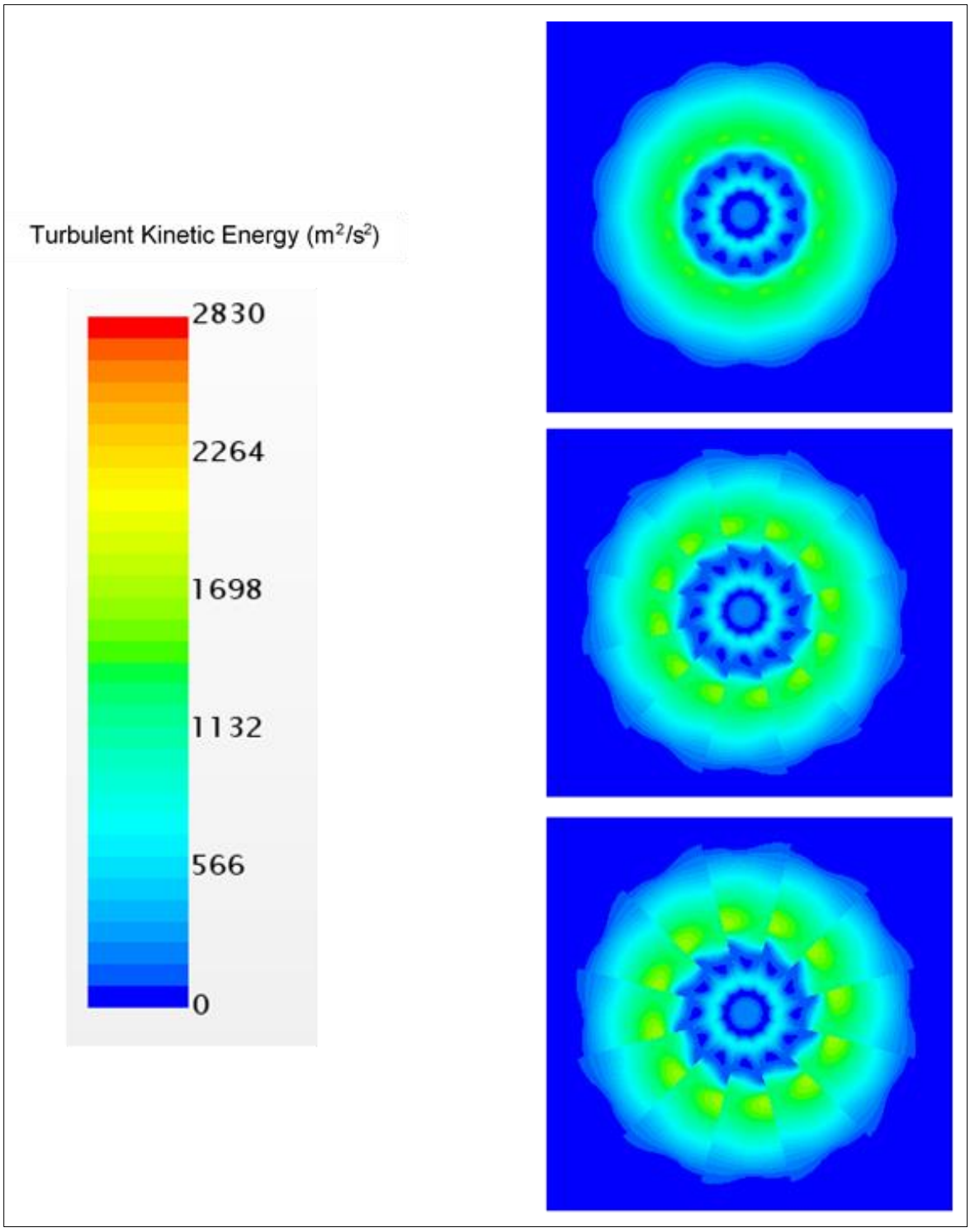

5.

Figure 3.28: Turbulent Kinetic Energy from the Chevron Nozzles at 3.1D_f Downstream (Top: 3I12I12, Middle: 3ITw12$_R$ITw12$_L$, Bottom: 3ITw12$_R$ITw12$_R$)

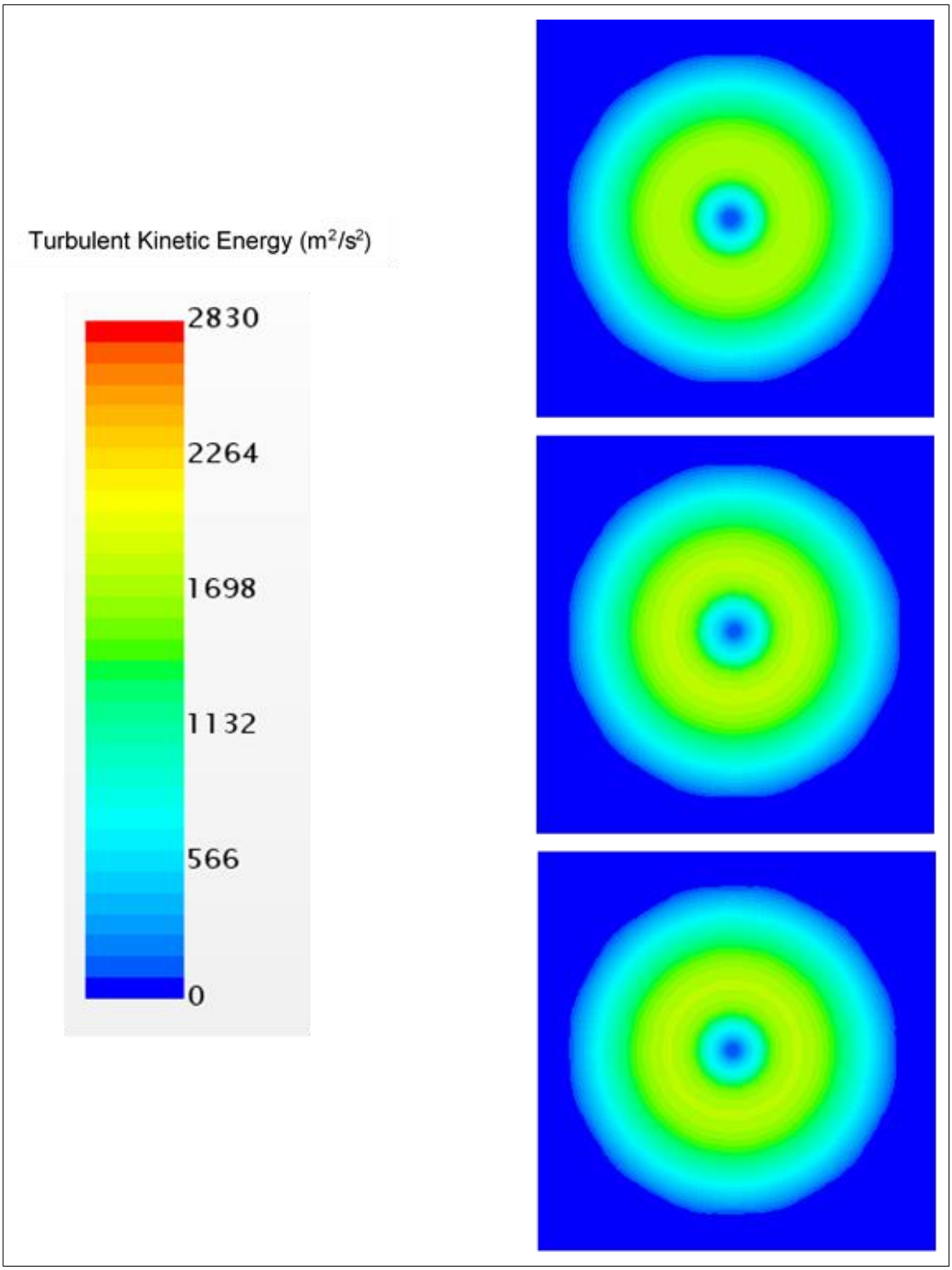

Figure 3.29: Turbulent Kinetic Energy from the Chevron Nozzles at 6.3D_f Downstream (Top: 3I12I12, Middle: 3ITw12$_R$ITw12$_L$, Bottom: 3ITw12$_R$ITw12$_R$)

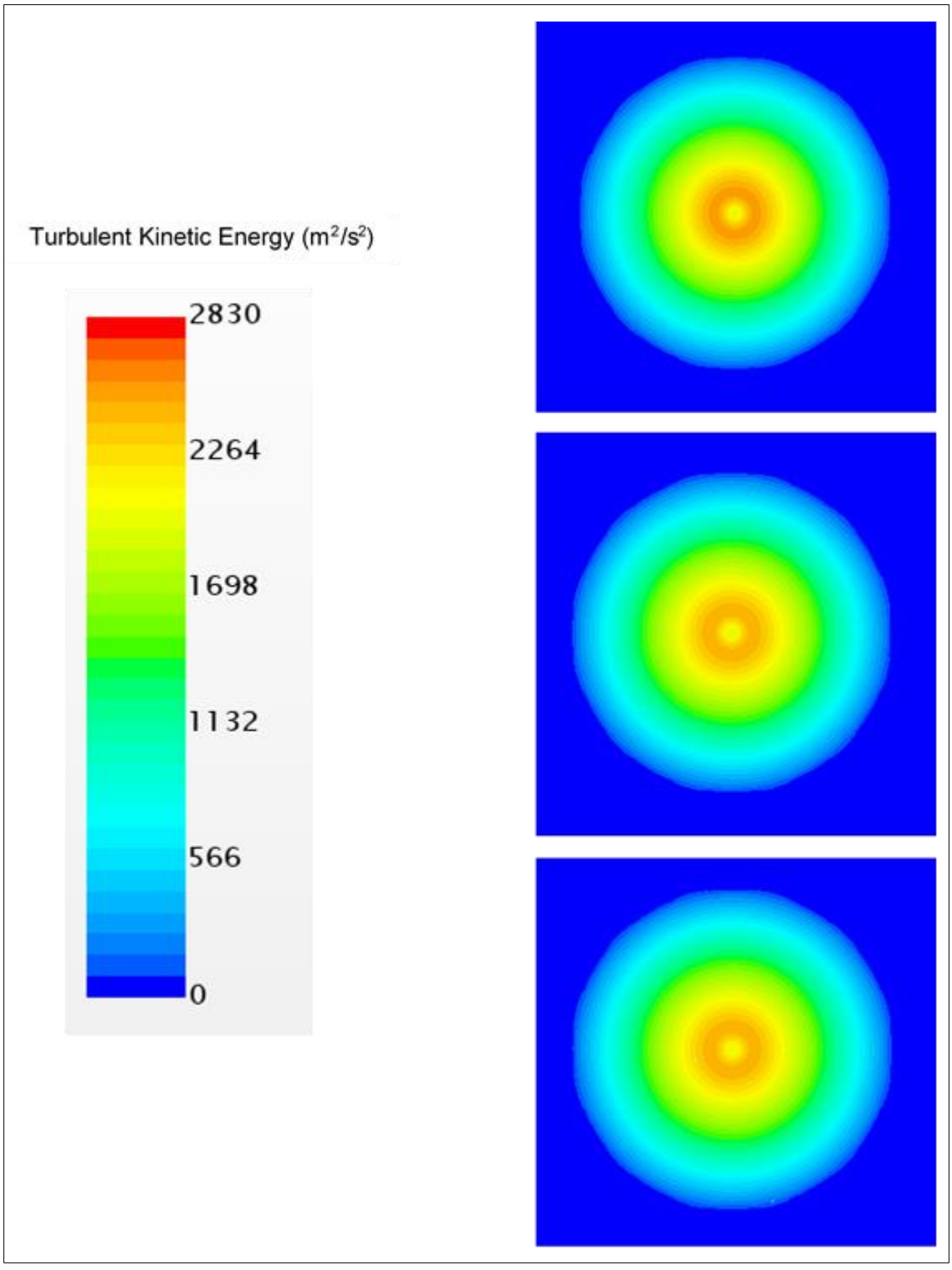

Figure 3.30: Turbulent Kinetic Energy from the Chevron Nozzles at 8.9D_f Downstream (Top: 3I12I12, Middle: 3ITw12$_R$ITw12$_L$, Bottom: 3ITw12$_R$ITw12$_R$)

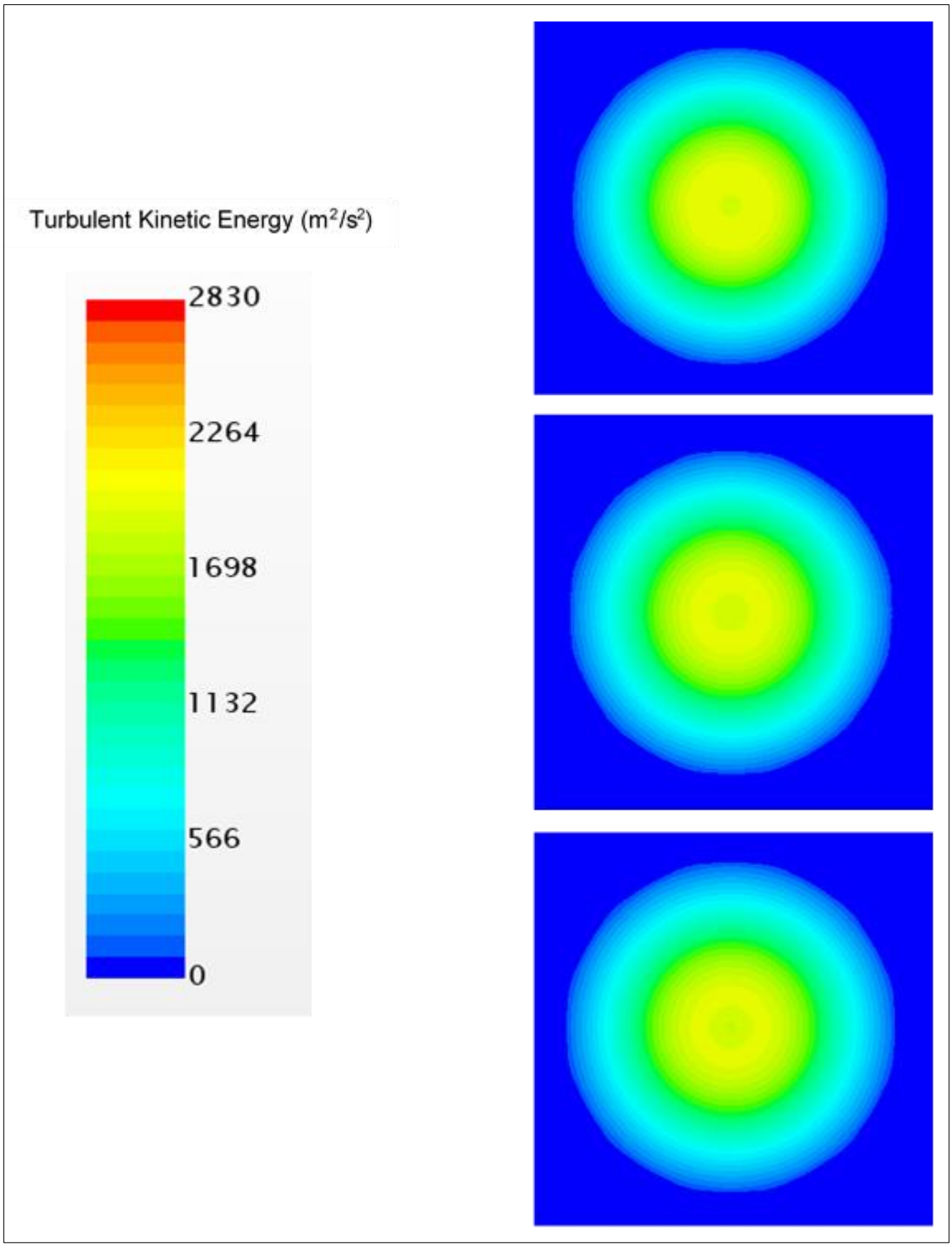

Figure 3.31: Turbulent Kinetic Energy from the Chevron Nozzles at 10.5D_f Downstream (Top: 3I12I12, Middle: 3ITw12$_R$ITw12$_L$, Bottom: 3ITw12$_R$ITw12$_R$)

Initially, at 1.1D_f downstream of each respective nozzle, the turbulent structure of the jet plume shows similar characteristics with noticeable differences between the structural forms that are

generated for the conventional and twisted chevrons. At this point, all chevron nozzles register approximately the same levels of turbulent kinetic energy. At $1.4D_f$ downstream, the $3ITw12_RITw12_L$ and $3ITw12_RITw12_R$ nozzles show comparable and slightly higher peaks in the TKE levels as compared to what is observed for the 3I12I12 nozzle. Up until this point, a clear distinction can be made between the core shear layer and the fan shear layer. At an axial location of $1.9D_f$ downstream, the first signs of the core and fan shear layers just starting to come into contact are visible. However, mixing between the two layers is still weak here.

At $3.1D_f$ downstream, in comparison to the 3I12I12 nozzle, higher levels of TKE are observed for the $3ITw12_RITw12_L$ and $3ITw12_RITw12_R$ nozzles in the fan and freestream mixing layers. Further downstream at $6.3D_f$, the turbulent structures for all three chevron nozzles begin to lose the spiral shape they earlier displayed. This essentially means that the vortices introduced by the chevrons now start to gradually dissipate. At this location, the three chevron nozzles display comparable levels of TKE. At a distance of $8.9D_f$ downstream of the nozzles, the spiraling structures observed upstream now transform into circles implying that the vortices from the chevrons have ceased to exist at this point. High levels of turbulent kinetic energy are observed here for each nozzle as the fan and freestream shear layers approach the axis. The 3I12I12 nozzle registers the highest level of turbulence with slightly lower levels being observed for the $3ITw12_RITw12_L$ and $3ITw12_RITw12_R$ nozzles. This location roughly corresponds to the axial distance downstream at which the turbulent kinetic energy peaks for each of the three chevron nozzles.

Finally, at $10.5D_f$ downstream, the turbulence in the jet plumes of the three chevron nozzles has diminished and similar levels of TKE are observed for all three nozzles. This indicates that the fan and freestream mixing layers have reached the axis at this stage. Among the three nozzles, the rate at which these layers approach the axis is observed to be the quicker for the $3ITw12_RITw12_L$ and the $3ITw12_RITw12_R$ nozzles with the quickest rate being seen in case of the $3ITw12_RITw12_R$ nozzle.

4. Conclusions

The numerical investigation of chevrons on subsonic jet flow is presented in this work. The study begins by first observing the performance of STAR-CCM+ in analyzing turbulent flows from subsonic nozzles. A laboratory scaled nozzle with a BPR of 5, termed the 3BB nozzle, chosen from NASA's AST program, is selected as the baseline model. The Shear Stress Transport (SST) k-ω turbulence model is chosen to run the simulation. The results of the numerical analysis for the baseline nozzle are presented in terms of the contours of the mean axial velocity and turbulent kinetic energy downstream of the nozzle and then compared with the PIV results for the same nozzle as presented by Bridges and Wernet [24]. Further, the jet velocity and total temperature along the centerline of the nozzle are plotted to gain more insight into the potential core of the jet. This data is also plotted against data available from the literature review. The results from the CFD analysis show a potential core that is slightly longer than what is observed by using the PIV technique. Further, the peak velocity in the jet is also relatively lower. However, in general, both, the PIV results and the results from STAR-CCM+ show a small region of recirculation in the flow shortly downstream of the external plug. This recirculation occurs due to the blunt trailing edge of the plug. The PIV and CFD data also show the jet spread to be similar.

In comparing the turbulent kinetic energy in the jet plume of the 3BB nozzle, it is observed that the SST k-ω turbulence model underpredicts the amount of turbulent kinetic energy reported through the use of PIV. While the peak value of the TKE found using the PIV method is 3500 m^2/s^2, the CFD analysis carried out on STAR-CCM+ demonstrates a peak value of approximately 2830 m^2/s^2. Although a mismatch in the turbulence is noticed here, the data from the numerical study relates closely with the CFD analysis carried out by Kenzakowski et al [26] using the CRAFT code. Kenzakowski used the k-ε turbulence model for the 3BB nozzle and reported a peak TKE value of about 2700 m^2/s^2. The work carried out on STAR-CCM+ here also shows that mixing between the fan and freestream shear layers dominates the flowfield. This is also observed in the images captured through the PIV technique in [24]. Weak mixing occurs between the core and fan shear layers and the jet plume resembles that of a typical turbofan.

To gain more insight into the potential core of the jet emanating from the baseline nozzle, the centerline velocity and total temperature profiles of the flow are analyzed. Both profiles are compared against available data from the literature survey. The SST k-ω model is seen to overpredict the length of the potential core when compared with the experimental data. However, the centerline velocity data from STAR-CCM+ shows a good overlap with some of the experimental results. Similar conclusions are drawn regarding the extent of the potential core when the centerline total temperature is plotted against the axial distance downstream, although the total temperature profile matches better with the experimental results in comparison to the centerline velocity profile. Further, in order to better understand the differences between the results from STAR-CCM+ and those from the CRAFT and WIND solvers, an error analysis is performed to see the overshoot in the normalized axial distances with respect to the centerline velocities and total temperatures. It is observed that, in general, the errors gradually diminish with increasing distance. Interestingly, after the potential core ends, STAR-CCM+ shows the steepest decline in the centerline velocity compared to the rates observed from the experimental and WIND data. However, in comparing the rates of decay of the total temperature, the rates are found to be almost the same for both, the STAR-CCM+ and CRAFT codes.

In general, STAR-CCM+ is found to be very suitable for the investigation of the turbulent class of jet flows. Some shortcomings do exist as are seen in the overprediction of the potential core and in the underprediction of the turbulent kinetic energy. However, those are the also observed in the work of others using other numerical software for the same purpose. Additionally, a few minor errors are also introduced owing to subtle differences between the geometric characteristics of the nozzles modeled using CAD and the actual nozzles used for experimental studies. Overall, the trends observed in parameters such as how the jet spreads along the axis and where mixing between the shear layers is the greatest, agree with the experimental data.

Once the performance of STAR-CCM+ in analyzing jet flows has been validated by using the baseline nozzle, it is now employed in the study of chevron nozzles. Two parametric designs of chevron nozzles, models $3ITw12_{R}ITw12_{L}$ and $3ITw12_{R}ITw12_{R}$, are presented that alter the shape of the conventional chevron. For comparative analysis, apart from the baseline nozzle, a conventional chevron nozzle, model 3I12I12, is also used. First, the centerline velocities and total temperatures downstream of each nozzle are graphed. The results indicate that the chevron

nozzles are able to reduce the potential core of the baseline nozzle from about 9 fan nozzle exit diameters to approximately 7 fan nozzle exit diameters. Further, the mean axial velocities seen downstream of the chevron nozzles are relatively lower than that observed for the 3BB nozzle. Among the three chevron nozzles, nozzle $3ITw12_RITw12_R$ shows the lowest mean axial velocity and the shortest potential core. Contours of the jet velocities and turbulent kinetic energy are also presented for the nozzles. These parameters are analyzed on two azimuthal planes where one plane passes the through a chevron tip (0° azimuthal plane) and the other through a chevron valley (15°). While the velocity contours for the chevron nozzles indicate a clear shortening of the length and mean width of the baseline nozzle's potential core, the effects of the chevrons are more pronounced on the 15° azimuthal plane where the $3ITw12_RITw12_R$ nozzle shows the shortest potential core and the 3I12I12 nozzle, the longest.

The comparison of the turbulent kinetic energy produced for each nozzle is particularly useful in this regard since it provides an idea about the amount of jet noise generated. In general, in comparison to the 3BB nozzle, all three chevron nozzles are successfully able to reduce the peak value of the turbulent kinetic energy in the flowfield by introducing vortices into the flow. The highest amounts of turbulence in the jet plumes of the chevron nozzles are also seen further upstream. Among the three chevron nozzles, although the peaks values of the turbulent kinetic energy are seen to be very close to each other, the new parametric nozzle designs produce relatively lower turbulence. Further, when it comes to the axial distance over which these high turbulent regions occur for each nozzle, it is seen that they are restricted to the smallest area for the $3ITw12_RITw12_R$ nozzle. Overall, the mixing of the fan and freestream shear layers still produces the greatest amount of turbulence. However, owing to the vortices introduced in the flow by the chevrons, the chevron nozzles generate much less turbulence that what is seen in case of the 3BB nozzle.

Thus, going by the theory that the turbulent kinetic energy directly relates to the amount of noise produced, it could be said that both, the $3ITw12_RITw12_L$ and the $3ITw12_RITw12_R$ nozzles, might produce the lowest jet noise among the nozzles considered in this work. This is evidenced by the lowest mean axial velocities downstream followed by the highest reduction in the peak value of the turbulent kinetic energy produced in the flowfield.

5. Recommendations

The numerical procedure carried out in this study makes use of the SST k-ω turbulence model. To expand on this work, a comparative analysis needs to be performed wherein different turbulence models in STAR-CCM+ are used to analyze the jet flow. This will provide a better understanding of how various models compare with the experimental data. Further, due to computational restrictions, the grids generated in this work are generated in a manner that the y+ values fall with the high y+ value range. In the future, low y+ values should be used for the same study for comparison purposes. Additionally, for the 3BB nozzle, a 3-D analysis should be performed followed by a comparison of the results with those available from the 2-D axisymmetric study presented herein.

The work documented in this work presents a preliminary analysis of the turbulence produced from chevron nozzles. The conclusion that the $3ITw12_{R}ITw12_{L}$ and $3ITw12_{R}ITw12_{R}$ nozzles might have the potential to produce the lowest jet noise here is inferred from the fact that the peak values of the turbulent kinetic energy in the jet plumes in this case are the lowest among the nozzles analyzed. However, no definitive statement can be made about how the chevrons affect the near-field or far-field noise. As a result, a full aeroacoustic analysis needs to be carried out through CFD. This will help to understand the kinds of frequencies being generated. Further, since thrust is a major determinant in analyzing the feasibility of a chevron nozzle, thrust calculations should be performed for all the nozzles analyzed in this work. A comparison of the amounts of thrust being produced will help to understand the performance of the nozzles better.

Finally, to aid the results available from the numerical investigation of these nozzles, laboratory scaled models should be manufactured and a live test be performed with the same boundary conditions stated in this study. This should be followed by a noise analysis at an acoustic facility so that the experimental results can be compared with those obtained from the numerical analysis. Further, the PIV technique could be implemented too, to better correlate the turbulent kinetic energy with the jet noise produced.

6. References

1. "*America on the Move*," National Museum of American History, Smithsonian Institution, n.d. Web.
2. Young, J., "*Mach Buster*," ChuckYeager.com, PMN III LLC, n.d. Web.
3. "*Aircraft Noise Reduction*," Development of Aviation Technology, Century of Flight, n.d. Web.
4. "*Stage 4 Aircraft Noise Standards*," Federal Register, Federal Aviation Administration, 01 Dec. 2003. Web.
5. "*Our Approach to Aircraft Noise Management*," Qantas Airways Limited, n.d. Web.
6. "*Aircraft Noise Issues*," Federal Aviation Administration, U.S. Department of Transportation, 29 Nov. 2016. Web.
7. "*Aircraft Noise Report 2015*," Federal Association of German Air Transport, n.d. Web.
8. Goldstein, M.E., "*Aeroacoustics*," NASA Scientific and Technical Information Office, Lewis Research Center, 1974.
9. Aizat. "*Using Technology to Combat Noise*," Silence, Please – On Noise Pollution, Blog Post, Centre for Instructional Technology, National University of Singapore, 13 Oct. 2016. Web.
10. Batard, H. "*Aircraft Noise Reduction: AIRBUS Industrial Needs In Terms Of New Materials For Nacelle Liners*," Journées scientifiques de l'ONERA, Airbus, 16 Jan. 2003. Presentation.
11. Leylekian, L., Lebrun, M., and Lempereur, P., "*An Overview of Aircraft Noise Reduction Technologies*," Aerospace Lab 7: 5, June 2014.
12. Kempton, A., "*Acoustic liners for modern aero-engines*," Rolls-Royce, 2011. Presentation.
13. Dobrzynski, W., "*Almost 40 Years of Airframe Noise Research – What Did We Achieve?*" Proceedings of the 14th Aeroacoustics Conference, 5-7 May 2008, Vancouver, Canada.
14. Kerrebrock, J.L., "*Aircraft Engines and Gas Turbines*," MIT Press, Cambridge, MA, 1977.
15. Lighthill, M.J. "*On Sound Generated Aerodynamically. I. General Theory*," Proceedings of the Royal Society A: Mathematical, Physical and Engineering Sciences 211(1107): 564-587, 20 Mar. 1952.

16. Mengle, V.G., Dalton, W.N., Bridges, J.C., and Boyd, K.C., "*Noise Reduction With Lobed Mixers: Nozzle-Length and Free-Jet Speed Effects*," 3rd AIAA/CEAS Aeroacoustics Conference, Atlanta, GA, 12-14 May 1997.
17. Rolls-Royce Plc, "*The Jet Engine*," 5th Edition, Rolls-Royce Technical Publications Department, 1996.
18. Bradbury, L.J.S., and Khadem, A.H., "*The Distortion of a Jet by Tabs*," Journal of Fluid Mechanics 70.04: 801-813, 1975.
19. Zaman, K.B.M.Q., and Foss, J.K., "*The effect of vortex generators on a jet in a cross-flow*," Physics of Fluids 9.1: 106-114, 1997.
20. Zaman, K.B.M.Q., Reeder, M.F., and Samimy, M., "*Control of an Axisymmetric Jet Using Vortex Generators*," Physics of Fluids 6.2: 778-793, 1994.
21. Zaman, K.B.M.Q., Bridges, J.E., and Huff, D.L., "*Evolution from 'tabs' to 'chevron technology' - a review*," Int. J. of Aeroacoustics 10.5 - 6: 685-710, 2011.
22. Janardan, B.A., Hoff, G.E., Barter, J.W., Martens, S., Gliebe, P.R., Mengle, V. and Dalton, W.N., "*AST Critical Propulsion and Noise Reduction Technologies for Future Commercial Subsonic Engines: Separate-Flow Exhaust System Noise Reduction Concept Evaluation*," NASA CR 2000-210039, 2000.
23. Saiyed, N.H., Mikkelsen, K.L., and Bridges, J.E., "*Acoustics and Thrust of Separate-Flow Exhaust Nozzles With Mixing Devices for High-Bypass-Ratio Engines*," NASA TM 2000-209948, 2000.
24. Bridges, J.E., and Wernet, M., "*Turbulence Measurements of Separate Flow Nozzles with Mixing Enhancement Features*," AIAA Paper 2002-2484, 8th AIAA/CEAS Aeroacoustics Conference, Breckenridge, Colorado, 17-19 June 2002.
25. Bridges, J., "*Measurements of Turbulent Flow Field in Separate Flow Nozzles With Enhanced Mixing Devices—Test Report*," NASA TM 2002-211366, 2002.
26. Kenzakowski, D.C., Shipman, J., Dash, S.M., Bridges, J.E., and Saiyed, N.H., "*Study of Three-Stream Laboratory Jets with Passive Mixing Enhancements for Noise Reduction*," AIAA Paper 2000-0219, 38th Aerospace Sciences Meeting and Exhibit, Reno, NV, 10-13 Jan. 2000.

27. Koch, L.D., Bridges, J., and Khavaran, A., "*Mean Flow and Noise Prediction for a Separate Flow Jet with Chevron Mixers,*" AIAA Paper 2004-0189, 42nd Aerospace Sciences Meeting and Exhibit, Reno, NV, 5-8 Jan. 2004.
28. Bridges, J., and Brown, C.A., "*Parametric Testing of Chevrons on Single Flow Hot Jets,*" AIAA Paper 2004-2824, 10th AIAA/CEAS Aeroacoustics Conference, Manchester, United Kingdom, 10-12 May 2004.
29. Callendar, B., Gutmark, E., and Martens, S., "*Far-Field Acoustic Investigation into Chevron Nozzle Mechanisms and Trends,*" AIAA J., 43(1): 87-95, 2005.
30. Callendar, B., Gutmark, E., and Martens, S., "*Near-Field Investigation of Chevron Mechanisms,*" AIAA J., 46(1): 36-45, 2008.
31. Kumar, S., "*Chevron Nozzle – Reduces EPN, and IR Signature of the Engine,*" LinkedIn.com, 22 Sep. 2016.
32. Kanmaniraja, R., Freshipali, R., Abdullah, J., Niranjan, K., Balasubramani, K., and Kumar, V. R. S., "*3D Numerical Studies on Jets Acoustic Characteristics of Chevron Nozzles for Aerospace Applications,*" Int. J. of Mechanical, Aerospace, Industrial, Mechatronic and Manufacturing Engineering, 8(9): 1530-1536, 2014.
33. Siemens Corporation, STAR-CCM+ v.11.02.010, 2016.
34. Siemens Corporation, STAR-CCM+ User Guide.
35. Thirumurthy, Deepak. "*Design and Analysis of Noise Suppression Exhaust Nozzle Systems,*" Thesis. Purdue University, May 2010. Web.
36. ANSYS, Inc., ANSYS FLUENT.
37. Menter, F. R., Kuntz, M., and Langtry, R., "*Ten Years of Industrial Experience with the SST Turbulence Model,*" Proceedings of the 4th International Symposium on Turbulence, Heat and Mass Transfer, Antalya, Turkey, 12 – 17 Oct. 2003.
38. Abramovich, G.N., "*The Theory of Turbulent Jets,*" 1st Edition, MIT Press, Cambridge, MA, 1963.